Assimilating synthetic hyperspectral sounder temperature and humidity retrievals to improve severe weather forecasts

Thomas A. Jones[1*], Steven Koch[2], Zhenglong Li[3]

[1.] Cooperative Institute for Mesoscale Meteorological Studies, University of Oklahoma, Norman, OK
[2.] NOAA National Severe Storms Laboratory, Norman, OK
[3.] Cooperative Institute for Meteorological Satellite Studies, University of Wisconsin, Madison, WI

Submitted to: Atmospheric Research
Revised: October 28, 2016

Corresponding Author Address:
Dr. Thomas A. Jones
Cooperative Institute for Mesoscale Meteorological Studies
University of Oklahoma
and
NOAA/OAR/National Severe Storms Laboratory
120 David L. Boren Blvd.
Norman, OK 73072
E-mail: Thomas.Jones@noaa.gov

Abstract

Assimilation of hyperspectral sounder data into numerical weather prediction (NWP) models has proven vital to generating accurate model analyses of tropospheric temperature and humidity where few conventional observations exist. Applications to storm-scale models are limited since the low temporal resolution provided by polar orbiting sensors cannot adequately sample rapidly changing environments associated with high impact weather events. To address this limitation, hyperspectral sounders have been proposed for geostationary orbiting satellites, but these have yet to be built and launched in part due to much higher engineering costs and a lack of a definite requirement for the data.

This study uses an Observation System Simulation Experiment (OSSE) approach to simulate temperature and humidity profiles from a hypothetical geostationary-based sounder from a nature run of a high impact weather event on 20 May 2013. The simulated observations are then assimilated using an ensemble adjustment Kalman filter approach, testing both hourly and 15 minute cycling to determine their relative effectiveness at improving the near storm environment. Results indicate that assimilating both temperature and humidity profiles reduced mid-tropospheric both mean and standard deviation of analysis and forecast errors compared to assimilating conventional observations alone. The 15 minute cycling generally produced the lowest errors while also generating the best 2-4 hour updraft helicity forecasts of ongoing convection. This study indicates the potential for significant improvement in short-term forecasting of severe storms from the assimilation of hyperspectral geostationary satellite data. However, more studies are required using improved OSSE designs encompassing multiple storm environments and additional observation types such as radar reflectivity to fully define the

effectiveness of assimilating geostationary hyperspectral observations for high impact weather forecasting applications.

1. Introduction

Many advancements in numerical weather prediction (NWP) have been made that can be attributed to the assimilation of satellite data to improve the analysis of the atmospheric state where traditional observations are not available (Derber and Wu, 1998; Le Marshall et al., 2007). Satellite observations include, but are not limited to, cloud-track winds (CTWs), retrieved temperature and humidity profiles, precipitation estimates, and recently lightning observations (Velden et al., 1998; Hou et al., 2004; Reale et al., 2008; Mansell et al., 2007; Schmitt et al., 2008). Each of these observation types can be assimilated into a NWP model to improve certain aspects of the model state. In recent years, assimilating information from hyperspectral sounders via infrared radiances or temperature and humidity retrievals has become a key component in NWP models (e.g., McNally et al., 2006; Reale et al., 2008; Li and Liu, 2009; Migliorini, 2012; Jones and Stensrud, 2012). One of the most significant limitations of NWP is the lack of observations describing the vertical structure of the atmosphere at high spatial and temporal scales. A partial solution to the current data void is provided by hyperspectral infrared spectrometers including the 2378-channel Atmospheric InfraRed Sounder (AIRS), the 8461-channel Infrared Atmospheric Sounding Instrument (IASI), and the 1305-channel Cross-track Infrared Sounder (CrIS). Temperature and humidity profiles can be retrieved from both instruments with high vertical resolution in clear to partly cloudy conditions from near the surface into the stratosphere (Aumann et al., 2003; Susskind et al., 2003; 2006). With such large channel sets, these instruments can substantially decrease the uncertainty of retrieved vertical profiles compared to other sounding instruments, which typically have no more than a few dozen channels.

Studies of assimilating retrieved profiles from polar orbiting sounders into NWP models have generally found a positive impact on model analyses and forecasts at various temporal and spatial scales (e.g., Le Marshall et al., 2006; Chou et al., 2007; Reale et al., 2008). Several studies focused on the impact of assimilating hyperspectral profiles on tropical cyclone track and intensity forecasts (Wu et al., 2006; Li and Liu, 2009; Liu and Li, 2010; Pu and Zhang, 2011; Atlas and Pagano, 2014). For example, Li and Liu (2009) and Liu and Li (2010) show an improvement to 12 – 96 hour track forecasts resulting from a better analyses of the mid-tropospheric temperature and mixing ratio while smaller, but still significant improvements, are present for intensity forecasts. Pu and Zhang (2011) found similar results while noting the possible need for bias adjustments in the assimilated profiles to further reduce forecast error. Additional research has been conducting focusing on the impacts of assimilating hyperspectral sounder profiles for severe weather events. Chou et al. (2010) describe an event in eastern Texas on 12-13 February 2007 in which AIRS profiles improved the characterization of the thermodynamic near storm environment leading to more accurate 6 hour precipitation forecasts. Jones and Stensrud (2012) further analyzed the impact of assimilating AIRS profiles on two Southern Plains events and found that even assimilating a single overpass of high-resolution temperature and humidity retrievals could significantly improve the analysis and forecast of the pre-storm environment, which should result in better forecasts of convective initiation and storm evolution. As in these cited severe weather studies, this research is primary concerned with the impact of retrievals on the representation of the environment, not the internal characteristics, of severe storms, and the subsequent impact on the evolution of the storms.

One key limitation of polar orbiting hyperspectral instruments is their poor temporal resolution relative to the time scales of high impact weather events. The importance of high temporal resolution hyperspectral information has been demonstrated by Aune et al. (2000), Schmitt et al. (2009) and Bingham et al. (2013). High impact weather events in particular are likely to be associated with a rapidly changing environment, which is poorly sampled by current observations. If the initial model representation of the environment is incorrect, then any potential forecasts will suffer. Even if the initial conditions are correct, it is unlikely the model will accurately capture the evolution of the near storm environment without high spatial and temporal resolution observations to update the model in a timely manner. A key hypothesis of this research is that improvements to the thermodynamic environment from assimilating hyperspectral sounder profiles translate to improvements in short-term forecasts of convection.

This research uses the Ensemble Adjustment Kalman Filter (EAKF) data assimilation scheme (e.g., Kalman, 1960; Anderson, 2001; Anderson and Collins, 2007; Yussouf and Stensrud, 2010), rather than the more traditional variational approach (e.g., Barker at al., 2004). The primary advantage of the EAKF approach is that it provides a flow dependent and dynamically evolving estimate of the multivariate background error covariances that is updated at each assimilation cycle. This is an important consideration for rapidly moving and developing weather phenomena and allows observations of one variable (say temperature) to influence other variables including those not observed (winds in the present study and potentially cloud microphysics variables).

Since there is no geostationary hyperspectral profiler that currently provides high spatial resolution temperature and humidity profiles over North America, this research uses the Observing System Simulation Experiment (OSSE) methodology to simulate such observations from a nature run and then to quantify impacts by comparing data assimilations and forecasts that include and exclude these data. Specifically, this study employs a “Quick OSSE” approach (Atlas et al., 2015) and an experimental setup similar to that of Jones et al. (2013a). Geostationary hyperspectral profilers would be expected to provide a temporal resolution of approximately 15 minutes with a spatial resolution on the order of 10 km or better. A case study approach is used based on the 20 May 2013 central Oklahoma (OK) tornado event that produced a violent tornado in Moore, OK and weaker, short lived tornadoes in southern OK. A very unstable, high shear environment was present over the Southern Plains during this day with convection forming along a frontal boundary in central OK and a connecting dryline further to the south. NWP experiments assimilating real radar and satellite observations of this event have shown some skill at forecasting the severe convection, but many uncertainties remain which were likely due to the lack of information on the near storm environment being assimilated in the model (Wheatley et al., 2016; Jones et al., 2016). An objective of this research is to assess whether assimilating near-storm environment information can, in fact, improve the model analyses, leading to better short-term (0-3 hour) forecasts of high impact weather events. However, these experiments only describe the impact for a single case using an OSSE system that is not fully validated and without the benefit of other high-resolution observations such as radar data. As a result, the applicability of these results to realistic settings remains uncertain.

Following this introduction, Section 2 describes the nature run created to simulate the 20 May 2013 event with Section 3 describing the synthetic simulated observations derived from the nature run. Section 4 provides an overview of the experiment design and Section 5 discusses the results of these data assimilation experiments. Finally, concluding remarks are given in Section 6.

2. Nature run

A nature run for the 20 May 2013 event was created from a deterministic forecast initialized from the Global Forecast System (GFS) analysis at 1200 UTC 14 May. The nominal GFS resolution in 2013 was 0.5° with 27 vertical levels which are downscaled to a 4 km resolution for the nature run. The nature run used a 1400 x 1200 grid point domain covering the continental United States (CONUS) with 56 vertical levels extending from the surface to 10 hPa (Fig. 1). The nature run was continuously integrated forward in time until 0000 UTC 21 May using the Advanced Weather Research Forecasting (WRF-ARW) model version 3.6.1 (Skamarock et al., 2008). Ferrier 3-class (cloud water, rain water, and snow mixing ratios) cloud microphysics is used along with GFDL shortwave and longwave radiation schemes, MYJ boundary layer physics, and the NOAH land surface model with 4 soil layers (Ferrier et al., 1996; Chou and Suarez, 1994; Janjic, 2002; Ek et al., 2003). Note that cumulus parameterization is unnecessary at a 4 km convection permitting resolution and is not used. Boundary conditions created from the operational GFS forecast initiated at 1200 UTC 14 May were applied at 3 hour intervals through the duration of the nature run. The length of the nature run is dictated by the need for the characteristics of the simulated 20 May event to be as independent from the initial conditions as possible, but still retain enough predictability to capture an event similar to that which occurred in reality.

3. Synthetic observations

Conventional and hyperspectral IR observations are simulated as described in the following. WSR-88D radar observations were not used in this study since the primary goal of this study is to isolate the impacts of assimilating high resolution satellite retrievals to the near storm environment. The impacts of assimilating radar reflectivity and Doppler radial velocity into high resolution NWP models is well understood and has been the focus of many studies. In particular, Wheatley et al. (2015) provide an overview of radar data assimilation for the 20 May event using a similar model configuration to the one being used here.

3.1. Conventional

Simulated observations are generated from the nature run for a variety of conventional observation types including Automated Surface Observing System (ASOS), Aircraft Communications Addressing and Reporting System (ACARS) and radiosonde instruments. For each ASOS location, 10 m wind speed and direction, 2 m temperature and humidity, and surface pressure observations are generated from the nature run at hourly intervals. Vertical profiles of temperature, humidity, and wind speed and direction are created to simulate radiosonde locations. Finally, simulated ACARS temperature, humidity, and wind observations are generated along real flight tracks. For all conventional observation types, location information reported in the Meteorological Assimilation Data Ingest Files (MADIS) at a particular analysis time is used. Observation measurement errors for each observation are drawn from unbiased, uncorrelated Gaussian error distributions that are based on a given sensor’s accuracy. For conventional observations, observation errors are based off those used the real-data system described by Wheatley et al. (2015) (Table 1).

3.2. Hyperspectral IR sounder

The synthetic atmospheric sounding retrievals are generated through a two-step process. In the first step, synthetic geostationary AIRS (GEO AIRS) radiances are simulated from the nature run (Aumann et al. 2003; Goldberg et al. 2003, 2004; Susskind et al. 2003, 2006). The GEO AIRS is assumed to replace the current GOES-13, 36,000 km above the equator at the longitude of -75 degree. The spatial resolution of the GEO AIRS is assumed to be exactly the same as the NR (4 km), but these data are thinned to 20 km to minimize the impact of representativeness error on the experiments. Xu (2011) showed that assimilating observations at a resolution of 2 times the model grid provides improved results and performance compared to assimilating observations at their full resolution. The temperature/moisture profiles, the surface skin temperature along with a climatology ozone profile and the UW Baseline Fit Emissivity database (Seemann et al., 2008) are used as input for the clear sky radiative transfer calculation using the Stand-Alone AIRS Radiative Transfer Algorithm (SARTA; Strow et al., 2003). SARTA has been successfully used in previous studies (Weisz, et al., 2007; Li et al., 2009; Smith et al., 2012). The cloudy radiances are simulated by coupling the clear sky SARTA transmittance with a cloudy radiance model developed by Wei et al. (2004). This model requires four parameters to calculate the cloud’s transmittance and scattering: the effective cloud particle size, the cloud optical thickness (COT), the cloud top pressure (CTP), and the cloud phase. All of this information can be determined from the nature run. This cloudy model coupled with SARTA is extremely fast in simulating cloudy radiances compared with the two other candidate radiative transfer models—the Community Radiative Transfer Model (CRTM; Chen et al., 2008) and the Radiative Transfer for TOVS (RTTOV; Saunders et al., 1999). Similar to the conventional observations, uncorrelated Gaussian errors are added to the simulated radiances based on real AIRS sensor specifications. These observation error standard deviations are then tuned to provide optimal ensemble data assimilation statistics such that the ratio of the standard deviation of the background spread in observation space to the standard deviation of the errors added to the simulated observations is near 1.0 (Xu et al., 2008). This is often labeled the consistency ratio (CR). Increasing the observation errors by a factor of 2.0 generated optimal CRs after the first few assimilation cycles. During testing, results were relatively insensitive to increasing the observation errors by factors from 1.5 to 2.5. The experiments described below all use these optimized observation errors (increased by the factor of 2.0).

In the second step, a simple linear regression based retrieval algorithm is used to retrieve the atmospheric sounding profiles from the nature run radiances. A randomly selected small subset (5%) of all the data is used as training to find the regression coefficients (Li et al., 2008, 2009). In an operational environment, these regression coefficients would be trained on sample of data from the previous days or weeks. To ensure consistent retrieval quality, channels affected by solar contamination as well as those with large observational noise are excluded. As a result, a subset of 1,148 channels were selected for use. The weighting functions of temperature and moisture for these channels using a randomly selected profile from the dataset is shown in Figure 2 (a,b). It is clear that the 1,148 channels provide a high vertical sampling density in the troposphere. In the mid-troposphere, the weighting functions are not only dense, but also display good sensitivity as depicted by the maximum absolute value of weighting functions. The predictors used for the retrievals include the brightness temperature (Tb), the brightness temperature squared (Tb^2), thereby accounting for non-linearity, and other know a priori variables such as the nature run surface pressure, local zenith angle, latitude etc. The predictands include the profiles of temperature and moisture, and the surface skin temperature. The logarithm of mixing ratio is used as the moisture predictand because it is more nearly linearly related to Tb.

For the cloudy regression, the four nature run cloud parameters are also used as predictands. Three sets of regression coefficients are generated, one for clear sky, one for water clouds, and one for ice clouds. In the retrieval, clear sky coefficients are applied to clear sky scenes, and cloudy coefficients are applied to cloudy scenes. The cloud mask is determined from the NR. This is likely to overestimate the impact from GEO AIRS. In reality, the cloud mask would be estimated from the brightness temperatures or by taking advantage of the high quality cloud mask product from the IR Imager on the same platform. During the experiment period, the cloud mask percentages for clear, water and ice clouds are 39%, 32%, and 29% respectively. Since no phase information is known before the retrieval in a real-world application, both sets of cloudy regression coefficients are applied. Each retrieval is used to calculate radiances, the best fit to the simulated observed radiances is chosen and the cloud phase is assigned accordingly. For both clear sky and cloud retrievals, a threshold of 0.8 K (explicitly determined as 2.5 times the instrument noise) is used to remove retrievals that do not pass quality control checks; if the spectrally averaged absolute difference between calculated and the synthetic radiances is larger than this threshold, it is considered of low quality and was abandoned for assimilation. As a result, only 22.2% of all the data are retained (15.7%, 5% and 1.5% for clear, water and ice clouds). Figure 2 (c and d) shows the high retrieval quality of the temperature and dewpoint as a function of height. Moreover, Figure 3 (a,b) shows these observations still have a very good coverage over the Southern Plains domain at 1800 UTC.

While the simulated retrieved profiles have 101 levels, this number far exceeds the amount of independent information present (Forsythe et al., 2015). The 8 vertical levels assimilated into the model are 100, 250, 400, 500, 600, 700, 800, and 900 hPa, which are similar to the independent levels reported in the standard AIRS retrieval product (Olsen et al., 2007).

Assimilating all levels retrieved below 500 hPa did not provide any significant advantages due to vertically correlated errors and the lower sensitivity of the radiances themselves to near surface conditions (not shown). The number of levels assimilated should be consistent with the vertical resolution of the model itself. Assimilating observations with near or better resolution than the model will not result in any benefit, and only acts to unnecessarily increase computational costs (Migliorini 2012). Prior to assimilation, mixing ratio observations and observation errors are converted to dewpoint as in Jones and Stensrud (2012), since dewpoint observation error has a more Gaussian distribution.

4. Experiment design

This research uses the ensemble data assimilation system described in detail by Wheatley et al. (2015). The main components of this data assimilation system are the WRF-ARW version 3.6.1 forecast model (Skamarock et al., 2008) and the Data Assimilation Research Testbed (DART) EAKF developed by NCAR (Anderson and Collins 2007; Anderson et al. 2009). The experimental setup follows the configuration employed by Wheatley and Stensrud (2010), Yussouf et al. (2013), and Jones et al. (2013b, 2015) with the following key details: A 385 x 265 horizontal grid at 12-km resolution with 56 vertical levels from approximately 20 m above the surface to 10 hPa using a total of 36 members (Fig. 1). All ensemble members use Thompson cloud microphysics (Thompson et al. 2004, 2008). Physics diversity is used for the remaining parameterization schemes to increase ensemble spread (Stensrud et al. 2000; Wheatley et al. 2015). Physics options include Kain-Fritsch, Grell, and Tiedtke cumulus parameterization schemes (outer domain only), YSU, MYJ, and MYNN boundary layer parameterizations, and Dudhia, RRTM, and RRTMG for the radiation (Table 2). The nature run uses MYJ, but otherwise uses different radiation schemes and since it is run at 4 km, no cumulus parameterization is used. One similarity between both the NR and assimilation model is the use of the 4-layer NOAH land surface model. Other potential land surface models were considered, but were found not to perform well in the real-data experiments of Wheatley et al. (2015) and Jones et al. (2016).

Using this model configuration, a “spin-up” experiment is initiated from the 1800 UTC 18 May GFS analysis and integrated forward in time 6 hours with no data assimilation. At 0000 UTC 19 May, hourly cycling begins, during which the simulated conventional observations described in Section 3.1 are assimilated on the 12 km grid. Note that radar, GPS/RO, and CTW observations were not included. Horizontal and vertical localization radii of 100 km and 4 km are applied to all conventional observations using the Gaspari and Cohn (1999) technique. Prior adaptive inflation (0.6) is also applied at each analysis cycle. Cycling continues until 1800 UTC 20 May, which represents the starting point for the hyperspectral temperature and humidity profile experiments described below.

Before undertaking these experiments, it is important to compare the final analysis of the spin up experiment at 1800 UTC to the nature run at this time (Fig. 4). Here, and in the figures and discussion that follow the analyses and forecasts are ensemble mean analyses and forecasts, unless otherwise specified. Overall, CNTL has a 1.0 K positive (warm) bias compared to the nature run with a RMSE of 1.5 K. This corresponds to a slight (0.4 g kg^{-1}) dry bias with a water vapor mixing ratio RMSE of 1.4 g kg^{-1}. At 1800 UTC, 20 May 2013, after 6.25 days of model integration, the nature run generates a large-scale 500 hPa trough over the central US with a base in New Mexico (Fig. 4a). A strong jet is evident with large areas of winds greater than 50 kt present. The greatest wind speeds (> 60 kt) lie in eastern Kansas (KS) and western Missouri. The

500 hPa flow is favorable for severe weather conditions over a large area from Texas (TX) northward to the Great Lakes. This study focuses on severe weather generated in the Southern Plains, particularly in Oklahoma (OK). The nature run surface temperature and wind analysis at this time shows an area of warm air in western TX and southwestern OK with cooler temperatures to the north and east (Fig. 4b). The cooler air is associated with morning cloud cover in eastern OK and precipitation in KS. A southwest – northeast oriented front is evident in northwestern OK with cool northerly winds behind and warm southerly winds ahead. Further south, the surface moisture analysis indicates the presence of a dryline in western OK corresponding to a sharp moisture gradient (Fig. 4c).

The vertical profile of temperature, dewpoint, and wind speed at 1800 UTC were extracted from the nature run at -97.44°W and 35.18°N, the location of the Norman, OK observing station (Fig. 5a). A strong capping inversion exists near 880 hPa preventing convection from forming at this time, but the capping inversion weakens over the next few hours. Surface-based CAPE is 3600 J kg^{-1}, which is more than enough to support severe convection. The vertical wind shear is also favorable except for weak winds in the 800 – 900 hPa layer. Wind speed in this layer increases as a function of time as the inversion weakens, thereby increasing 0-1 km storm relative helicity to > 250 m^2 s^{-2} and priming the atmosphere for severe convection to develop.

The 500 hPa patterns in the spinup analysis valid at 1800 UTC are broadly similar to that of the nature run with both depicting a large scale trough and high wind speeds along its base. The spin up wind speeds are generally ~10 kt less than the corresponding nature run values for two reasons (Fig. 4a,c). First, the nature run is a 4 km resolution model whereas the domain plotted from the spin up experiment is a 12 km run; thus, it is not as likely to resolve the highest wind speed values. Second, the ensemble mean averages out the highest winds speeds in individual members since their exact location is not constant from member to member. Overall surface conditions are also similar between the nature run and spin up experiment. The boundaries between surface warm and cool air are located in the same area of the Southern Plains (Fig. 4b,d). The spin up experiment is slightly warmer at the surface compared to the nature run. The surface moisture characteristics are also consistent between the nature run and spin up experiment (Fig. 4c,f). The vertical profiles of temperature, humidity and wind at the location of the Norman, OK observing station are also similar except that the weakness in wind near 800 hPa in the nature run is not as evident in the experiment (Fig. 5b). The overall similarity between the spin up experiment and nature run, while also containing several detailed differences, indicates the data assimilation experiments are also likely to be capable of representing severe convection and the environmental conditions which could support severe convection, which is a necessary requirement for this research to be successful.

Four experiments are conducted to assess the impacts of assimilating simulated hyperspectral temperature and humidity profiles into a mesoscale model using the EAKF approach. The simulated profiles are also assimilated on the 12 km grid and use horizontal and vertical localization radii of 100 and 3 km respectively. All experiments are initialized from the spin up run at 1800 UTC 20 May 2013 and cycled forward in time at 15 minute intervals until 0000 UTC 21 May, with the exception that the control (CNTL) experiment assimilates no additional data. The CNTL experiment is still cycled since cycling itself can result in a somewhat different result than if an uninterrupted 6 hour forecast were run from the 1800 UTC analyses. The CONV1H experiment assimilates simulated conventional observations at hourly intervals and is essentially a continuation of the spin up experiment. Hourly simulated temperature and humidity retrievals are added to form the PROF1H experiment. Finally, the PROF15M experiment assimilates 15 minute resolution retrievals along with the hourly conventional observations. Observations are split into 15 minute chunks with a nominal ±7.5 minute window around each 15 minute assimilation time use to determine valid observations. Thus, PROF15M assimilates approximately 4 times the number of observations than does PROF1H. PROF15M is performed to determine if the high temporal resolution of future geostationary satellite-based hyperspectral sounder retrievals have a meaningful advantage over a lower temporal resolution product for the case studied here. Forecasts are generated from each experiment beginning at 2000 and 2100 UTC and integrated out to 0000 UTC 21 May. Each forecast is run in a one-way nested configuration with an inner 4 km domain centered over the Southern Plains (Fig. 1). The model configuration remains the same as the outer 12 km domain with the exception that cumulus parameterization is no longer applied. The higher resolution of the inner grid allows for better representation of convection than possible at a 12 km resolution and is directly comparable to the 4 km resolution nature run. No data assimilation occurs on the inner 4 km domain.

5. Results

5.1. Assimilation cycle difference statistics

The first step in determining the effectiveness of assimilating simulated temperature and humidity profiles is to calculate the mean and RMS of the innovation (observation minus background) and residual (observation minus analysis) for each assimilation cycle to assess the overall fit of the background and analysis compared to the observations (Dowell et al. 2004; Dowell and Wicker 2009). When plotted as a time series, these statistics often show a saw-tooth pattern in which mean and RMS differences increase during the forecast cycle from analysis to subsequent background only to be reduced again by the next analysis. Figure 6 shows mean and RMS differences for temperature and dewpoint for the CNTL, PROF1H, and PFOH15M experiments. Approximately 70,000 temperature and dewpoint observations are assimilated during each cycle. No assimilation occurs in CNTL; thus, the magnitude of the differences either remain constant or increase as a function of time. Mean CNTL temperature differences vary from -0.3 K to -0.5 K by 0000 UTC, indicating that the CNTL experiment becomes increasingly warmer than the observations as a function of time (Fig. 6a). The corresponding RMS differences also increases in magnitude, from 1.0 to 1.2 K, over the same time period (Fig. 6b). For dewpoint, CNTL generates a relatively constant mean difference of -1.7 K, indicating the experiment is slightly moister than the observations (Fig. 6c). The corresponding RMS differences for dewpoint range between 4.0 – 4.3 K (Fig. 6d). The CONV1H experiment (not shown) is very similar to the CNTL experiment since neither assimilates the simulated temperature and humidity retrievals.

Assimilating simulated temperature and humidity profiles at hourly intervals in PROF1H reduces the magnitude of the mean and RMS differences for both parameters. At each analysis time, the magnitude of the mean differences decreases by 0.05 K with a corresponding decrease in RMS difference of 0.1 K. The cumulative impact of assimilating the profile observations on temperature is an approximately 50% reduction of the RMS innovation of 0.4 K by 2300 UTC compared to CNTL. Even greater relative impacts were observed for dewpoint temperature. During the first analysis, the magnitude of the mean dewpoint difference decreases by 85% from -1.7 K to only -0.26 K, though it increases slightly in later assimilation cycles (Fig. 6c). Corresponding RMS differences stabilize near 2.0 K after 2000 UTC, which is less than 50% of the CNTL RMS differences (Fig. 6d). Assimilating observations at 15-minute intervals

(PROF15M) has an even greater positive impact. For temperature, the mean differences are only -0.15 K by the end of the assimilation period (a 70% reduction), while RMS innovation stabilizes near 0.6 K (Fig. 6a,b). The dewpoint mean difference for PROF15M are approximately 0.2 K smaller in magnitude compared to PROF1H and the RMS innovations are smaller by over 0.5 K after the first few assimilation cycles (Fig. 6c, d). The greatest impacts from data assimilation occur during the first hour of the assimilation period. Once the analysis has been modified to better match the simulated observations, the data assimilation appears to retain that information, reducing later analysis residuals.

5.2. Potential temperature and water vapor differences

The spatial distribution of the differences between perturbation potential temperature (i.e. potential temperature minus 300 K) and water vapor indicate where assimilating simulated temperature and humidity profiles have their greatest impact. Figure 7a shows the difference between 5 km AGL perturbation potential temperature difference computed as the difference between the nature run and the corresponding ensemble mean analysis temperature from CNTL over the Southern Plains domain at 2000 UTC (Nature minus CNTL). To calculate this difference, the 4 km nature run is re-sampled to the 4 km nest domain of the experiments. Over the northern portion of the domain, the nature run is generally cooler than CNTL while it is somewhat warmer in southeastern OK. Assimilating simulated observations should adjust the model towards the nature run through the appropriate warming and cooling increments.

To assess the impact of assimilating the simulated observations, the difference between ensemble mean potential temperature between CNTL and the other experiments (Experiment minus CNTL) are calculated in the same fashion. For CONV1H, the overall differences are small given the limited number of simulated upper air observations being assimilated. CONV1H is slightly cooler (~1K) in northern OK with other small-scale differences in central OK associated with the developing convection (Fig. 7b). Assimilating temperature and humidity profiles at hourly intervals generates far larger differences. PROF1H is cooler compared to CNTL in KS while it is warmer in the western portion of the domain (Fig. 7c). In addition, PROF1H is warmer in eastern OK. The spatial patterns of the differences roughly correspond to those present between the nature run and CNTL. PROF15M generates a similar spatial pattern of potential temperature differences as does PROF1H, but the magnitude of the differences are often higher (Fig. 7c,d).

Figure 8 shows the corresponding 5 km water vapor mixing ratio difference at 2000 UTC between the nature run and CNTL (a) and CNTL and the experiments (b,c,d). The nature run is generally dryer than CNTL over much of the domain with the only exception occurring near the location of early convection in north-central OK (Fig. 8a). Hourly assimilation of conventional observations only (CONV1H) results in small differences in water vapor compared to CNTL (Fig. 8b). Much larger differences are generated by PROF1H and PROF15. Both are dryer than CNTL in the same areas where the nature run is dryer than CNTL (Fig. 8c,d) indicating that assimilating the simulated temperature and humidity profiles are adjusting the moisture in the experiment closer to the nature run value. The magnitude of the drying is somewhat larger in PROF15M compared to PROF1H, consistent with the temperature difference results (Figs. 7d, 8d). This indicates that more frequent assimilation has a larger impact, which is fully consistent with the lower temperature and dewpoint differences and RMSEs shown previously.

5.3. Atmospheric impacts

The impact of assimilating temperature and humidity retrievals is clearly evident from the vertical profile of ensemble mean temperature and dewpoint at the OUN sounding site for the nature run and each of the 4 experiments at 2000 UTC (Fig. 9). The impact on the temperature profile is small since all the experiments, even CTRL perform quite well, especially above 800 hPa. Much larger differences are present in the moisture profiles. Between 600 – 400 hPa, CNTL and CONV1H both overestimate humidity compared to the nature run. However, PROF1H and PROF15M both closely match the nature run in this layer indicating that assimilating moisture profiles in particular is effective at reducing mid-level moisture errors in the model.

The vertical distribution of the analysis and forecast errors (i.e., Experiment minus Nature) for the entire 4 km domain are calculated to confirm the result shown above. The bias or mean error and root mean square error (RMSE) for perturbation potential temperature and water vapor mixing ratio are calculated for each layer for each ensemble member. In Figs. 10 and 11, the ensemble mean and standard deviation of the layer statistics (bias and RMSE) are plotted as symbols and error bars. These error bars provide an estimate of the overall *ensemble spread* in layer bias and RMSE.

Figure 10 shows bias and RMSE for temperature and water vapor mixing ratio for the 2000 UTC analysis. First, regarding the temperature impacts, below 500 hPa, all the experiments are warmer than the nature run, with the largest warm bias occurring near the surface (Fig. 10a). CNTL has the largest bias while PROF15 has the lowest within this layer. Below 850 hPa, most of the improvement over CNTL is due to assimilation of conventional surface observations (CONV1H) and not profiler observations. An experiment similar to PROF15, but without the conventional observations, also resulted in little improvement compared to CNTL at low levels (not shown). Above 850 hPa, the impact of the temperature and humidity profiles is larger. In most cases, the PROF15 lowers the bias relative to PROF1H, though the magnitude of the difference is small. Between 500 – 200 hPa, both CNTL and CONV1H have a cool bias, which is removed in PROF1H and PROF15M, though the spread in bias is quite large in this layer. PROF1H and PROF15M also decrease temperature RMSE over CNTL and CONV1H in the 800 – 200 hPa layer (Fig. 10c). The magnitude of the improvement is greatest near 450 hPa. Also note that the standard deviation in RMSE for both PROF1H and PROF15M is quite small and lies outside the standard deviation of RMSE from the other experiments throughout most of the 800 – 200 hPa layer.

Next we examine the bias and RMSE for tropospheric water vapor. These error statistics are both reduced by assimilating simulated hyperspectral retrieved profiles. The improvement is most evident in the middle troposphere (600 – 400 hPa) where CNTL and CONV1H have a moist bias, which is substantially reduced in PROF1H and PROF15M (Fig. 10b). RMSE is improved over a deeper layer between 800 – 400 hPa (Fig. 10d). Recall that many of the peak weighting functions for atmospheric temperature and moisture sensitivity generally occur in the mid-to-upper troposphere (Fig. 2), which is similar to the level where the maximum improvement in bias occurs. Thus, the greatest positive impacts occur where the sensor is most sensitive to moisture, which would be the expected and desirable result.

While assimilating temperature and humidity profiles have a significant impact on the analyses, whether or not these impacts are retained in forecasts is even more important. If the model quickly reverts back to the pre-assimilation conditions, then assimilating the temperature and humidity profiles would not be useful. Fortunately, the impacts are still clearly evident in 4-h forecasts valid at 0000 UTC 21 May (Fig. 11) initiated from the 2000 UTC analyses (Fig. 10). Both PROF1H and PROF15M continue to reduce bias and RMSE for temperature compared to

CNTL though the ensemble spread is larger since this is a 4 hour forecast (Fig. 11a,d). Both these experiments cool the atmosphere compared to CNTL and CONV1H at heights up to 300 hPa. The cooling impact is slightly larger in PROF15M, which is due to the more frequent data assimilation and consistent with the differences in the 2000 UTC analyses. However, the additional cooling between 500 – 300 hPa actually results in a colder bias relative to PROF1H indicating that assimilating more data is not always optimal. The reduction in moisture bias between 600 – 400 hPa also remains, but the improvement in RMSE becomes small (Fig. 11b,d). Conversely, the difference in bias between CNTL and PROF1H / PROF15M for u-wind has decreased, but the reduction in RMSE remains (not shown). Overall, it is clear that at least some information assimilated from the profiler data is being retained at least 4 hours into the forecast which in turn should impact the forecast of severe convection within the model. The overall vertical bias and error profiles for temperature and humidity are broadly similar at 2000 UTC and the 4 hour forecast at 0000 UTC with one major exception. At 0000 UTC all forecasts generate a dry bias relative to the nature run between 800 – 700 hPa indicating that the depth of the moisture is likely being underestimated by these experiments. Assimilating simulated profiles did little to alter this feature.

5.4. Reflectivity forecasts

To visualize the impact of the storm environment changes resulting from assimilating simulated temperature and humidity profiles, the ensemble mean 3 km AGL reflectivity analysis at 2000 UTC and hourly forecasts for CONV1H, PROF1H, and PROF15M are compared to the nature run reflectivity over the Southern Plains. The nature run reflectivity shows the progression of convective development from around the time of convective initiation to when convection becomes widespread (Fig. 12). Convection begins to develop by 2000 UTC with two areas of convection developing in central OK and north TX (Fig. 12a). The coverage and intensity of the convection in both regions increase further by 2100 UTC (Fig. 12b). Development of both areas continues over the next 3 hours with additional convection forming in between the original two areas (Fig. 12c-e). The strongest convection in the nature run during the 2100 – 0000 UTC time period appears to occur over central OK, which is consistent the placement of the actual tornadic supercell that occurred on 20 May 2013.

CONV1H generate two areas of convection, one in central OK, and the other on the boarder of OK and TX at 2000 UTC (Fig. 12f), which is broadly similar to the nature run analysis at this time (Fig. 12a). The detailed characteristics of simulated radar reflectivity differ considerably, but this is due to the much more complex cloud microphysics used in the experiments from which more accurate representations of reflectivity can be derived and the fact that the ensemble averaging smears out the storm structures in the individual ensemble members. This latter effect is particularly evident in the blue edges of the ensemble averages due to the spread in the placement of the ensemble storm boundaries. As forecast time increases, storm coverage increases with both areas of storms maintained out to 0000 UTC, which is consistent with the nature run. However, the coverage and location is not an exact match, leaving room for improvement from assimilating temperature and humidity profiles.

PROF1H generates reflectivity analyses at 2000 and 2100 UTC similar in appearance to the CONV1H with the exception of lower ensemble mean reflectivity values associated with the southern area of convection (Fig. 12f,g,k,l). Larger differences emerge by 2200 UTC, or 2 hours into the forecast, as PROF1H generates higher ensemble mean reflectivity values in central OK, which indicate that this experiment is generating stronger convection and lower overall ensemble spread (Fig. 12m). This difference remains throughout the remainder of the forecast period. Assimilation of temperature and humidity profiles at 15 minute intervals further impacts the model forecasts. At 2000 and 2100 UTC, PROF15M generates weaker storms than either CONV1H or PROF1H (Fig. 12). However, this changes by 2200 UTC, after which PROF15M generates the highest reflectivity values. The reason PROF15M suppresses convection relative to the other experiments is due to 15 minute assimilation of what are mostly cloud-free or at best partly cloudy observations. In particular, all the humidity observations assimilated are sub-saturated. The more frequent the assimilation, the greater the impact of these sub-saturated observations have on nearby saturated areas. Thus, while the environment is improved, convection initiation is inhibited. (See further discussion in the Conclusions.)

5.5. Updraft helicity forecasts

One of the key goals of this research is to determine if assimilating hyperspectral temperature and humidity profiles can improve the forecasts of rotating supercell storms. To examine this question, 2-5 km updraft helicity is compared between the nature run and each experiment. Updraft helicity (UH) is a diagnostic parameter designed for tracking rotation in model-simulated storms that is computed by taking the integral of the vertical vorticity multiplied by the updraft velocity between 2 and 5 km AGL (Kain et al. 2008). The probability of UH greater than 50 $m^2\ s^{-2}$ is calculated for each experiment over the 0-4 hour forecast period beginning at 2000 UTC and compared with the location of nature run UH greater than 50 $m^2\ s^{-2}$. Probability is calculated using the 3-by-3 grid point neighborhood around a particular horizontal model grid point for each member at a given time in which UH exceeds the above threshold divided by the total number of ensemble members. The maximum probability recorded at each horizontal gridpoint during the entire 4 hour forecast period is shown (Figs. 13 and 14).

The nature run generates two areas of UH greater than 50 m^2 s^{-2} between 2000 – 0000 UTC located in central OK and north TX (hatched areas in each panel of Fig. 13). CONV1H generates UH probabilities greater than 40% associated with the central OK storm, and greater than 60% for the southern storm during this period (Fig. 13a). However, both UH tracks are displaced north and east of the UH generated in the nature run. PROF1H reduces the northern displacement bias for the central OK storm to some degree, but is otherwise quite similar to PROF1H (Fig. 13b). PROF15M differs from the other two experiments by generating greater than 40% near the UH present in the nature run for the central OK storm (Fig. 13c). Further south, PROF15M appears to decrease UH probabilities compared to the other two experiments. PFOF15M also generates a third area of UH just to the southwest of the area in central OK corresponding to a signal also present in the nature run.

The differences between these experiments increase for 3 hour forecasts initiated at 2100 UTC. Both CONV1H and PROF1H again generate UH probabilities greater than 40% corresponding to the central OK storm, but the placement of the UH swaths is well to the north and east of the nature run (Fig. 14). Conversely, PROF15M generates a large swath of UH probabilities greater than 60% very near to the corresponding nature run for the central OK storm track, representing a significant improvement compared to PROF1H. These results indicate that the changes to the near-storm environment through assimilating simulated temperature and humidity profiles can have a positive impact on their forecasts.

6. Conclusions

Assimilating synthetic hyperspectral temperature and humidity profiles using an EAKF approach reduced mid-tropospheric temperature and humidity misfits to the observations and errors compared to an experiment that only assimilated conventional observations. The greatest improvement occurs at the first assimilation cycle after which smaller improvements occur as cycling continues. Assimilating synthetics profiles at hourly intervals proved successful, but 15 minute cycling generally produced somewhat smaller biases and errors compared to the hourly cycling experiments. The improvements persist several hours into the forecast period after data assimilation has ceased.

The impacts to the near-storm environment resulted in large differences in the forecast evolution of convection within the model. The 15 minute cycling experiments generally produced the most skillful forecasts of reflectivity and updraft helicity in the 2-4 hour time period. However, the 15 minute experiments did have difficulty spinning up convection compared to the hourly and even conventional data only experiments. It is likely that assimilating only data in cloud-free areas at high temporal intervals has the unwanted impact of suppressing nearby cloud cover and precipitation since the influence of clear-sky observations extends beyond the observation location. While this result is concerning, this problem would be significantly reduced if information relating to clouds and precipitation were also assimilated into these experiments. Any real-time, operational NWP model designed for high weather impact forecasts would likely include this information and would likely reduce the negative impact to convective initiation caused by the assimilation of large amounts of cloud-free data. The preliminary experiments describe here suggest that as improved spatial and temporal resolution hyperspectral data become available, their importance in improving forecasts of high weather impacts will increase.

This research only represents a preliminary study of the impact of geostationary hyperspectral observations to severe weather forecasting and significant additional research is required to fully understand and quantify the potential impact. Future experiments should utilize a higher resolution OSSE run over an extended time period, or for several cases, containing multiple severe weather events. The new OSSE should also use advanced cloud microphysics so that other high resolution observations of cloud and precipitation properties such as radar reflectivity can be simulated. Further improvements to the treatment of partly cloudy radiances and retrievals is also required. Thus, while the results shown for this example are indeed promising, much more work is required to determine their overall applicability to high impact weather forecasting.

Acknowledgements

We thank the journal reviewers for their thoughtful and insightful comments. This material is based upon work supported by the US Weather Research Program within NOAA/OAR Office of Weather and Air Quality. Partial funding was provided by NOAA/Office of Oceanic and Atmospheric Research under NOAA-University of Oklahoma Cooperative Agreement #NA11OAR4320072, U.S. Department of Commerce.

References

Anderson, J. L., 2001. An ensemble adjustment filter for data assimilation. *Mon. Wea. Rev.*, **129**, 2884–2903.

——, 2007. An adaptive covariance inflation error correction algorithm for ensemble filters. *Tellus*, **59A**, 210-224.

——, 2009. Spatially and temporally varying adaptive covariance inflation for ensemble filters. *Tellus*, **61A**, 72-83.

Anderson, J. L., and Collins, N. 2007. Scalable implementations of ensemble filter algorithms for data assimilation. *J. Atmos. Oceanic Technol*., **24**, 1452-1463.

Anderson, J. L., Hoar, T., Raeder, K., Liu, H., Collins, N., Torn, R., and Avellano, A. 2009. The Data Assimilation Research Testbed: A community data assimilation facility. *Bull. Amer. Meteor. Soc*., **90**, 1283–1296.

Atlas, R. and T. S. Pagano, 2014. Observing system simulation experiments to assess the potential impact of proposed satellite instruments on hurricane prediction. Imaging Spectrometry XIX, P. Mouroulis and T. S. Pagano, Eds., Society of Photo-Optical Instrumentation Engineers, Bellingham, WA, Proceed. SPIE, Vol. 9222, 9 pp. doi:10.1117/12.2063648.

Atlas, R., L. Bucci, B. Annane, R. Hoffman, and S. Murillo, 2015. Observing system simulation experiments to assess the potential impact of new observing systems on hurricane forecasting. Marine Technology Society Journal, 49 (6), 140–148, doi:10.4031/MTSJ.49.6.3. Special issue, Evolution of Marine Technologies: Commemorating the 50th Anniversary of the MTS Journal, guest edited by Donna Kocak.

Aumann, H. H., Chahine, M. T., Gautier, C., Goldberg, M. D., Kalnay, E., McMillin, L. M., Revercomb, H., Rosenkranz, P. W., Smith, W. L., Staelin, D. H., Strow, L. L., and Susskind, J. 2003. AIRS/AMSU/HSB on the Aqua mission: Design, science objectives, data products and processing systems. *IEEE Trans. Geosci. Remote Sens*., **41** (2), 253–264.

Aune, R. M.,Menzel, W. P., Thom, J., Bayler, G. M., Huang, A., and Antonelli, P. 2000. Preliminary findings from the geostationary interferometer observing system simulation experiments (OSSE). NOAA Tech. Rep. NESDIS 95, 18 pp.

Barker, D. M., Huang, W., Guo, Y.-R., and Xiao, Q. N. 2004. A Three-Dimensional (3DVAR) Data Assimilation System For Use With MM5: Implementation and Initial Results. *Mon. Wea. Rev*., **132**, 897-914.

Bingham, G., et al., 2013. Rapidly updated hyperspectral sounding and imaging data for severe storm prediction. Infrared Remote Sensing and Instrumentation XXI, Society of Photo-Optical Instrumentation Engineers, Bellingham, WA, Proceed. SPIE, Vol. 8867, 14 pp. Paper 886702. doi:10.1117/12.2030687.

Chen Y., Weng, F., Han, Y., and Liu, Q., 2008. Validation of the Community Radiative Transfer Model by using CloudSat data. *J. Geophys. Res*., **113**, D00A03, doi:10.1029/2007JD009561.

Chou, M.-D., and Suarez, M. J. 1994. An efficient thermal infrared radiation parameterization for use in general circulation models. NASA Tech. Memo. 104606, 85pp. [Available from NASA Center for Aerospace Information, 800 Elkridge Landing Road, Linthicum Heights, MD 21090-2934.].

Chou, S-H., B. Zavodsky, G. Jedlovec, and W. Lapenta, 2007. Assimilation of atmospheric infrared sounder (AIRS) profiles using WRF-VAR. NCAR, *9th Annual WRF Users' Workshop*, **P5.14**, Boulder, CO.

Chou, S-H., B. Zavodsky, and G. Jedlovec, 2010. Regional precipitation forecast with Atmospheric InfraRed Sounder (AIRS) profile assimilation. *11th Annual WRF Users' Workshop, Boulder, CO*.

Derber, J. C., and Wu, W.-S. 1998. The Use of TOVS cloud-cleared radiances in the NCEP SSI analysis system. *Mon. Wea. Rev*., **126**, 2287-2299.

Dowell, D., F. Zhang, L. J. Wicker, C. Snyder, and N. A. Crook, 2004. Wind and temperature retrievals in the 17 May 1981 Arcadia, Oklahoma, supercell: Ensemble Kalman filter experiments. *Mon. Wea. Rev*., **132**, 1982–2005.

Dowell, D. C., and L. J. Wicker, 2009. Additive noise for storm- scale ensemble forecasting and data assimilation. *J. Atmos. Oceanic Technol*., **26**, 911–927.

Dudhia, J., 1989. Numerical study of convection observed during the Winter Monsoon Experiment using a mesoscale two- dimensional model. *J. Atmos. Sci*., **46**, 3077–3107.

Ek, M., Mitchell, K. E.,Lin, Y., Rogers, E., Grunmann, P., Koren, V., Gayno, G., and Tarpley, J. D. 2003. Implementation of Noah land surface model advances in the National Centers for Environmental Prediction operational mesoscale Eta Model. *J. Geophys. Res*., **108**, 8851, doi:10.1029/2002JD003296.

Ferrier, B. S., Simpson, J., and Tao, W.-K. 1996. Factors Responsible for Precipitation Efficiencies in Midlatitude and Tropical Squall Simulations. *Mon. Wea. Rev*., **124**, 2100–2125.

Forsythe, J. M., S. Q. Kidder, K. K. Fuell, A. LeRoy, G. J. Jedlovec, and A. S. Jones, 2015. A multisensor, blended, layered water vapor product for weather analysis and forecasting. *J. Operational Meteor*., 3 (5), 41□58, doi: http://dx.doi.org/10.15191/nwajom.2015.0305.

Gaspari, G., and Cohn, S. E. 1999. Construction of correlation functions in two and three dimensions. *Quart. J. Royal Meteor. Soc.,* **125**, 723-757.

Goldberg, M.D., Y. Qu, L.M. McMillin, W. Wolf, L. Zhou, and M. Divakarla, 2003. AIRS near-real-time products and algorithms in support of operational numerical weather prediction. *IEEE Trans. Geosci. Remote Sensing*, **41**, 379-389.

Goldberg, M. D., C. D. Barnet, W. Wolf, L. Zhou, and M. Divakarla 2004. Distributed real-time operational products from AIRS, paper presented at SPIE International Symposium on Optical Science and Technology. 49th Annual Meeting, Int. Soc. Opt. Eng., Denver, Colo.

Hou, A. Y., Zhang, S. Q., and Reale, O. 2004. Variational continuous assimilation of TMI and SSM/I rain rates: Impact on GEOS-3 hurricane analyses and forecasts. *Mon. Wea. Rev*., **132**, 2094-2109.

Janjic, Z. I. 2002. Nonsingular implementation of the Mellor–Yamada level 2.5 scheme in the NCEP Meso model. NCEP Office Note 437, 61 pp.

Jones, T.A. and Stensrud, D.J, 2012. Assimilating AIRS temperature and mixing ratio profiles using an Ensemble Kalman Filter approach for convective-scale forecasts. *Wea. and Forecasting*, **27**(3), 541-564.

Jones, T. A., J. Otkin, D. J. Stensrud, and K. Knopfmeier, 2013a. Assimilation of satellite infrared radiances and Doppler radar observations during a cool season Observing System Simulation Experiment. Mon. Wea. Rev. 141, 3273–3299.

Jones, T. A., D. J. Stensrud, P. Minnis, and R. Palikonda, 2013b. Evaluation of a forward operator to assimilate cloud water path into WRF-DART. *Mon. Wea. Rev.*, **141**, 2272–2289.

Jones, T. A., D. J. Stensrud, L. Wicker, P. Minnis, and R. Palikonda, 2015. Simultaneous radar and satellite data storm-scale assimilation using an ensemble Kalman filter approach for 24 May 2011. *Mon. Wea. Rev*. **143**, 165–194.

Jones, T. A., Knopfmeier, K., Wheatley, D., Creager, G., Minnis, P., and Palikondo, R. 2016. The NSSL Multiscale Ensemble. Part 2: Combined radar and satellite assimilation. *Wea. Forecasting*, **31**, 297-327.

Kain, J. S., Weiss, S. J., Bright, D. R., Baldwin, M. E., Levit, J. J., Carbin, G. W., Schwartz, C. S., Weisman, M. L., Droegemeier, K. K., Weber, D. B., and Thomas, K. W. 2008. Some Practical Considerations Regarding Horizontal Resolution in the First Generation of Operational Convection-Allowing NWP. *Wea. Forecasting*, **23**, 931–952.

Kalman, R.E., 1960. A new approach to linear filtering and prediction problems. *Journal of Basic Engineering*, **82**, 35–45.

Le Marshall, J., J. Jung, J. Derber, M. Chahine, R. Treadon, S. J. Lord, M. Goldberg, W. Wolf, H. C. Liu, J. Joiner, J. Woollen, R. Todling, P. van Delst, Y. and Tahara, 2006: Improving global analysis and forecasting with AIRSImproving global analysis and forecasting with AIRS. *Bull. Am. Meteorol. Soc*., **87**, 891–894.

Le Marshall, J., Uccellni, L., Eiaudi, F., Colton, M., Chang, S., Wang, F., Uhart, M., Lord, S., Riishojgaard, L-P., Phoebus, P., and Yoe, J. G. 2007. The Joint Center for Satellite Data Assimilation. *Bull. Am. Meteorol. Soc*., **88**, 329–340.

Li, J. and Liu H. 2009. Improved hurricane track and intensity forecast using single field-of-view advanced IR sounding measurements. *Geophys. Res. Lett*., **36**, L11813, doi:10.1029/ 2009GL038285.

Li, Z., Li, J., Menzel, W. P., Nelson III, J. P., Schmit, T. J.,Weisz, E., and Ackerman, S. A. 2009. Forecasting and nowcasting improvement in cloudy regions with high temporal GOES sounder infrared radiance measurements, *J. Geophys. Res*., **114**, D09216, doi:10.1029/2008JD010596.

Li, Z., Li, J., Menzel, W. P., Schmit, T. J., Nelson III, J. P., Daniels, J., and Ackerman. S. A. 2008. GOES sounding improvement and applications to severe storm nowcasting, *Geophys. Res. Lett.*, **35**, L03806, doi:10.1029/2007GL032797.

Lin, X., and K. G. Hubbard, 2004. Sensor and electronic biases/ errors in air temperature measurements in common weather station networks. J. Atmos. Oceanic Technol., 21, 1025–1032.

Liu, H. and Li, J. 2010. An Improvement in Forecasting Rapid Intensification of Typhoon Sinlaku, 2008: Using Clear-Sky Full Spatial Resolution Advanced IR Soundings. *J. Appl. Meteor. and Clim.*, **49**, 821 – 827.

Liu, J., Li, H., Kalnay, E., Kostelich, E. J., and Szunyogh, I. 2009. Univariate and multivariate assimilation of AIRS humidity retrivals with the local ensemble transform Kalman filter. *Mon. Wea. Rev.*, **137**, 3918-3932.

Mansell, E., Ziegler C., and MacGorman, D. 2007. A lightning data assimilation technique for mesoscale forecast models. *Mon. Wea. Rev.*, **135**, 1732–1748.

McNally, A. P., Watts, P. D., Smith, J. A., Engelen, R., Kelly, G. A., Thepaut, J. N., and Matricardi, M. 2006. The assimilation of AIRS radiance data at ECMWF, *Quart. J. Roy. Meteor. Soc*., **132**, 935–957.

Meng, Z. and Zhang, F. 2011. Limited area ensemble based data assimilation: A review. *Mon. Wea. Rev.*, **139**, 2025 – 2045.

Migliorini, S. 2012. On the equivalence between radiance and retrieval assimilation. *Mon. Wea. Rev*., **140**, 258–265.

Olsen, E. T., and Coauthors. 2007. AIRS/AMSU/HSB version 5 data release user guide. [Available online at http://disc.sci.gsfc.nasa.gov/AIRS/documentation/v5_docs/].

Pagano, T. S., Aumann, H. H., Hagan, D. E., and Overoye, K. 2003. Pre- launch and in-flight radiometric calibration of the Atmospheric Infrared Sounder (AIRS), *IEEE Trans. Geosci. Remote Sens.*, **41**, 265–273.

Pu, Z. and Zhang, L. 2011. Validation of AIRS Temperature and Moisture Profiles Over Tropical Oceans and Their Impact on Numerical Simulations of Tropical Cyclones. *J. Geophys. Res.*, **115**, D24114, doi:10.1029/2010JD014258.

Reale O., Susskind, J., Rosenberg, R., Brin, E., Liu, E., Riishojgaard, L. P., Terry, J., and Jusem, J. C. 2008. Improving forecast skill by assimilation of quality-controlled AIRS temperature retrievals under partially cloudy conditions. *Geophys. Res. Lett*., **35**, L08809, doi:10.1029/2007GL033002.

Saunders, R., Matricardi, M., and Brunel, P. 1999. An improved fast radiative transfer model for assimilation of satellite radiance observations, *Quart. J. Roy. Meteor. Soc*, **125**, 1407-1425.

Schmit, T. J.; Li, J., Gurka, J. J., Goldberg, M. D., Schrab, K. J., Li, J. and Feltz, W. F. 2008. The GOES-R Advanced Baseline Imager and the continuation of current sounder products. *J. Appl. Meteor. and Climatol*., **47**(10), 2696-2711. http://dx.doi.org/10.1175/2008JAMC1858.1.

Schmit, T. J.; Li, J., Ackerman, S. A. and Gurka, J. J. 2008. High-spectral- and high-temporal-resolution infrared measurements from geostationary orbit. *J. Atmos. and Oceanic Tech*., **26**(11), 2273-2292. http://dx.doi.org/10.1175/2009JTECHA1248.1.

Seemann, S.W., Borbas, E. E., Knuteson, R. O., Stephenson, G. R., Huang, H.-L. 2008. Development of a Global Infrared Land Surface Emissivity Database for Application to Clear Sky Sounding Retrievals from Multi-spectral Satellite Radiance Measurements. *J. Appl. Meteor. Climatol.*, **47**, 108-123.

Skamarock, W. C., Klemp, J. B., Dudhia, J., Gill, D. O., Barker, D. M., Duda, M. G., Huang, X-Y., Wang, W. and Powers, J. G. 2008. A description of the Advanced Research WRF version 3. NCAR Tech Note NCAR/TN-475+STR, 113 pp. [Available from UCAR Communications, P. O. Box 3000, Boulder, CO 80307.]

Smith, W. L., Weisz, E., Kirev, S., Zhou, D. K., Li, Z. and Borbas, E. E. 2012. Dual-regression retrieval algorithm for real-time processing of satellite ultraspectral radiances*, J. Appl. Meteorol. Clim.*, **51**(8), 1455–1476.

Strow, L. L., Hannon, S. E., De Souza-Machado, S., Motteler, H. E., and Tobin, D. 2003. An overview of the AIRS radiative transfer model. IEEE Trans. Geosci. Remote Sens., 41, 303– 13.
Susskind, J., C. D. Barnet, and J. M. Blaisdell, 2003: Retrieval of atmospheric and surface parameters from AIRS/AMSU/HSB data in the presence of clouds. *IEEE Trans. Geosci. Remote Sens.*, **41**, 390–409.

Susskind, J., C. D. Barnet, and J. M. Blaisdell, 2003. Retrieval of atmospheric and surface parameters from AIRS/AMSU/HSB data in the presence of clouds. IEEE Trans. Geosci. Remote Sens., 41, 390–409.

Susskind, J., Barnet, C., Blaisdell, J., Iredell, L., Keita, F., Kouvaris, L., Molnar, G., and Chahine, M. 2006. Accuracy of geophysical parameters derived from Atmospheric Infrared Sounder/Advanced Microwave Sounding Unit as a function of fractional cloud cover. *J. Geophys. Res.*, **111**, D09S17, doi:10.1029/2005JD006272.

Thompson, G., Rasmussen, R. M., and Manning, K. 2004. Explicit forecasts of winter precipitation using an improved bulk microphysics scheme. Part I: Description and sensitivity analysis. *Mon. Wea. Rev*., **132**, 519–542.

——, Field, P. R., Rasmussen, R. M., and Hall, W. R. 2008. Explicit forecasts of winter precipitation using an improved bulk microphysics scheme. Part II: Implementation of a new snow parameterization. *Mon. Wea. Rev*., **136**, 5095–5115.

Velden, C. S., Olander, T. L., Wanzong, S. 1998. The impact of multispectral GOES-8 wind information on Atlantic tropical cyclone track forecasts in 1995. Part 1: Dataset methodology, description and case analysis. *Mon. Wea. Rev*., **126**, 1202-1218.

Wei, H., Yang, P., Li, J., Baum, B. B., Huang, H., Platnick, S., Hu, Y., and Strow, L. 2004. Retrieval of semitransparent ice cloud optical thickness from Atmospheric Infrared Sounder (AIRS) measurements, *IEEE Trans. Geosci. Remote Sens*., **42**, 2254 – 2267, doi:10.1109/ TGRS.2004.833780.

Weisz, E., Li, J., Li, J., Zhou, D., Huang, H., Goldberg, M. D., and Yang, P. 2007. Cloudy sounding and cloud top height retrieval from AIRS alone single field-of-view radiance measurements, *Geophys. Res. Lett*., **34**, L12802, doi:10.1029/2007GL030219.

Wheatley, D. M., and Stensrud, D. J., 2010. The impact of assimilating surface pressure observations on severe weather events in a WRF mesoscale ensemble system. *Mon. Wea. Rev*., **138**, 1673-1694.

Wheatley, D. M., Knopfmeier, K., Jones, T. A., Creager, G. 2015. Storm-scale Data Assimilation and Ensemble Forecasting with the NSSL Experimental Warn-on Forecast System. Part I: Radar Data Experiments., *Wea. and Forecasting*. **30**, 1795–1817.

Wu, L., Braun, S. A., Qu, J.J., and Hao X., 2006. Simulating the formation of Hurricane Isabel (2003) with AIRS data. *Geophys. Res. Lett*., **33**, L04804, doi:10.1029/2005GL024665.

Xu, Q., 2011. Measuring information content from observations for data assimilation: Spectral formulations and their implications to observational data compression. Tellus, 63A, 793–804.

Xu, Q., Huijuan, L., Gao S., Xue, M., and Tong, M, 2008. Time-Expanded Sampling for Ensemble Kalman Filter: Assimilation Experiments with Simulated Radar Observations. Mon. Wea. Rev., 136, 2651–2667, doi: 10.1175/2007MWR2185.1.

Yussouf, N., and Stensrud, D. J. 2010. Impact of Phased-Array Radar Observations over a Short Assimilation Period: Observing System Simulation Experiments Using an Ensemble Kalman Filter. *Mon. Wea. Rev*., **138**, 517-538.

Yussouf, N., E. R. Mansell, L. J. Wicker, D. M. Wheatley, D. J. Stensrud, 2013. The ensemble Kalman filter analyses and forecasts of the 8 May 2003 Oklahoma City tornadic supercell storm using single- and double-moment microphysics schemes. *Mon. Wea. Rev*., **141**, 3388–3412.

Figure Captions

Figure 1. Geographical domains of the 4 km resolution nature run (NATURE), the 12 km horizontal resolution mesoscale experiments (EXP), and the 4 km nest (NEST) used for verification against the nature run.

Figure 2. Temperature (a) and dewpoint (b) vertical weighting functions for the simulated GEO_AIRS instrument. The standard deviation (STDDEV) of the retrieval error of (c) temperature and (d) moisture (dewpoint) for simulated observations passing quality control.

Figure 3. Synthetic temperature (a) and water vapor mixing ratio (b) retrievals at 800 hPa at 1800 UTC over the Southern Plains domain. White areas indicate where no retrievals were possible due to high clouds.

Figure 4. (a) Wind speed (knots) and direction at 500 hPa, (b) surface (2 m) temperature and 10 m winds, and (c) surface (2 m) water vapor mixing ratio for the nature run at 1800 UTC 20 May. Panels d, e, and f are identical, but for the spin-up ensemble mean analysis. The black dot indicates the location of Norman, OK (OUN) and the black and red lines indicate the approximate locations of the front and dryline respectively.

Figure 5. Temperature, dewpoint, and wind speed and direction profiles from (a) the Nature run and (b) the spin-up analysis located at Norman, OK (OUN) at 1800 UTC 20 May.

Figure 6. Mean (left panels) and RMSE (right panels) innovations (observations minus background) and residuals (observation minus analysis) for (top) temperature and (bottom) dewpoint temperature for CNTL, PROF1H, and PROF15M experiments for each assimilation cycle between 1800 UTC 20 May and 0000 UTC 21 May.

Figure 7. Potential temperature differences at 5 km and 2000 UTC 20 May with respect to the CNTL analysis for (a) the nature run (Nature), and for the (b) CONV1H, (c), PROF1H, and (d) PROF15M ensemble mean analyses.

Figure 8. Water vapor mixing ratio difference at 5 and 2000 UTC 20 May with respect to the CNTL analysis for (a) the nature run (Nature), and for the (b) CONV1H, (c), PROF1H, and (d) PROF15M ensemble mean analyses.

Figure 9. Vertical profile of temperature, dewpoint, and wind speed (kt) for each ensemble mean analysis and for the nature run at 2000 UTC at Norman OK (OUN).

Figure 10. Vertical profiles of temperature and water vapor mixing ratio mean errors (top) and RMSE (bottom) for the 4 km nest for the 2000 UTC analysis. The mean and RMSE are calculated at each level for each ensemble member. Then the ensemble mean and standard deviations of these statistics are plotted as lines and error bars, respectively.

Figure 11. Same as Figure 10, but for a 4 hour forecast valid at 0000 UTC 21 May.

Figure 12. Simulated radar reflectivity at 3 km AGL from the nature run at 2000 (a), 2100 (b), 2200 (c, 2300 (d), and 0000 UTC (e) 20 May. Ensemble mean radar reflectivity at 3 km AGL for the 2000 UTC analysis and following forecasts at 2100, 2200, 2300, and 0000 UTC for CONV1H, PROF1H, and PROF15 experiments (f-t).

Figure 13. Ensemble estimated probability of 2-5 km updraft helicity integrated over a 4 hour forecast initiated at 2000 UTC 20 May greater than 50 m^2 s^{-2} for (a) CONV1H, (b) PROF1H, and (c) PROF15 experiments. In each panel the hatched areas indicate location of nature run helicity greater than 50 m^2 s^{-2} over the same time period.

Figure 14. Same as Figure 14, but a for 3 hour forecasts initiated at 2100 UTC.

Figures

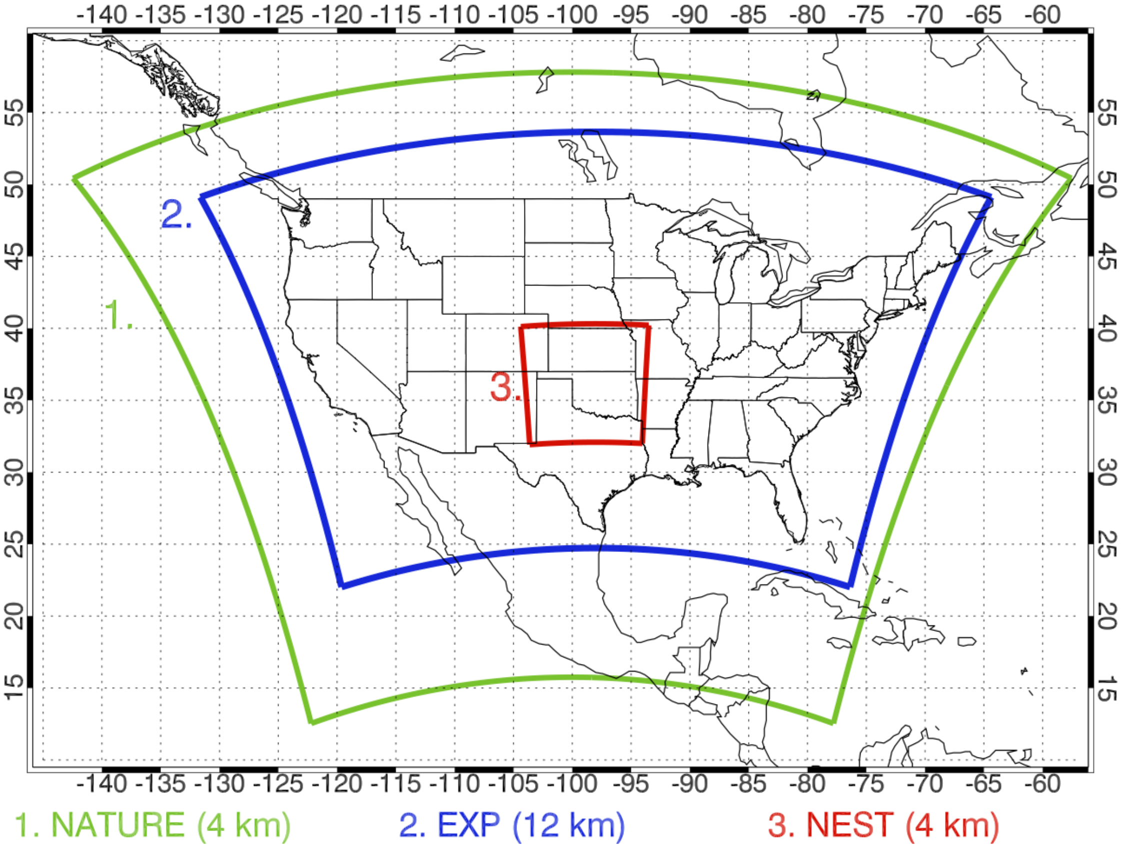

Figure 1. Geographical domains of the 4 km resolution nature run (NATURE), the 12 km horizontal resolution mesoscale experiments (EXP), and the 4 km nest (NEST) used for verification against the nature run.

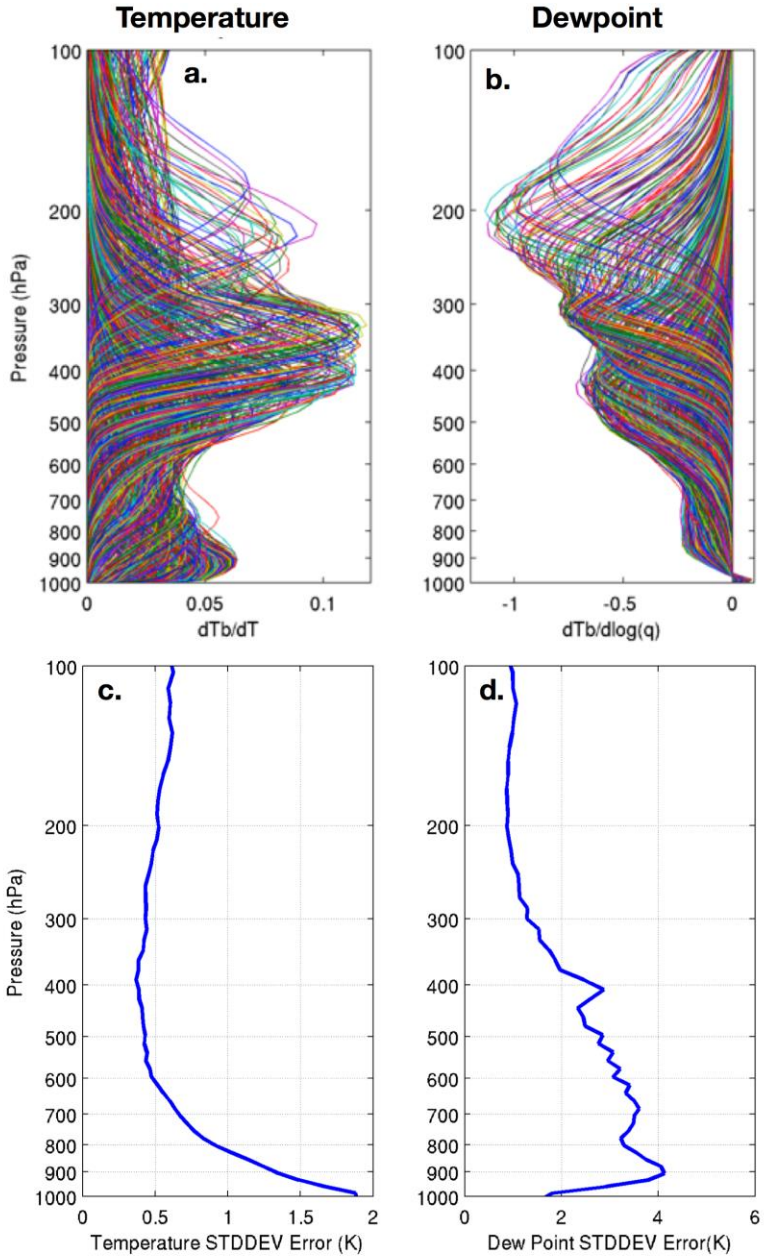

Figure 2. Temperature (a) and dewpoint (b) vertical weighting functions for the simulated GEO_AIRS instrument. The standard deviation (STDDEV) of the retrieval error of (c) temperature and (d) moisture (dewpoint) for simulated observations passing quality control.

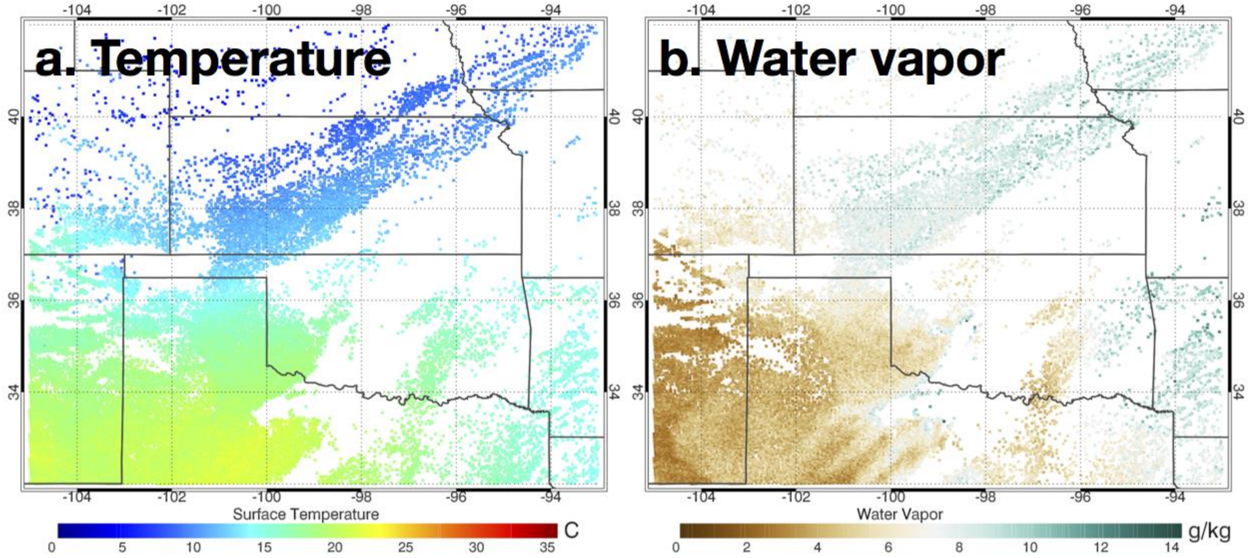

Figure 3. Synthetic temperature (a) and water vapor mixing ratio (b) retrievals at 800 hPa at 1800 UTC over the Southern Plains domain. White areas indicate where no retrievals were possible due to high clouds.

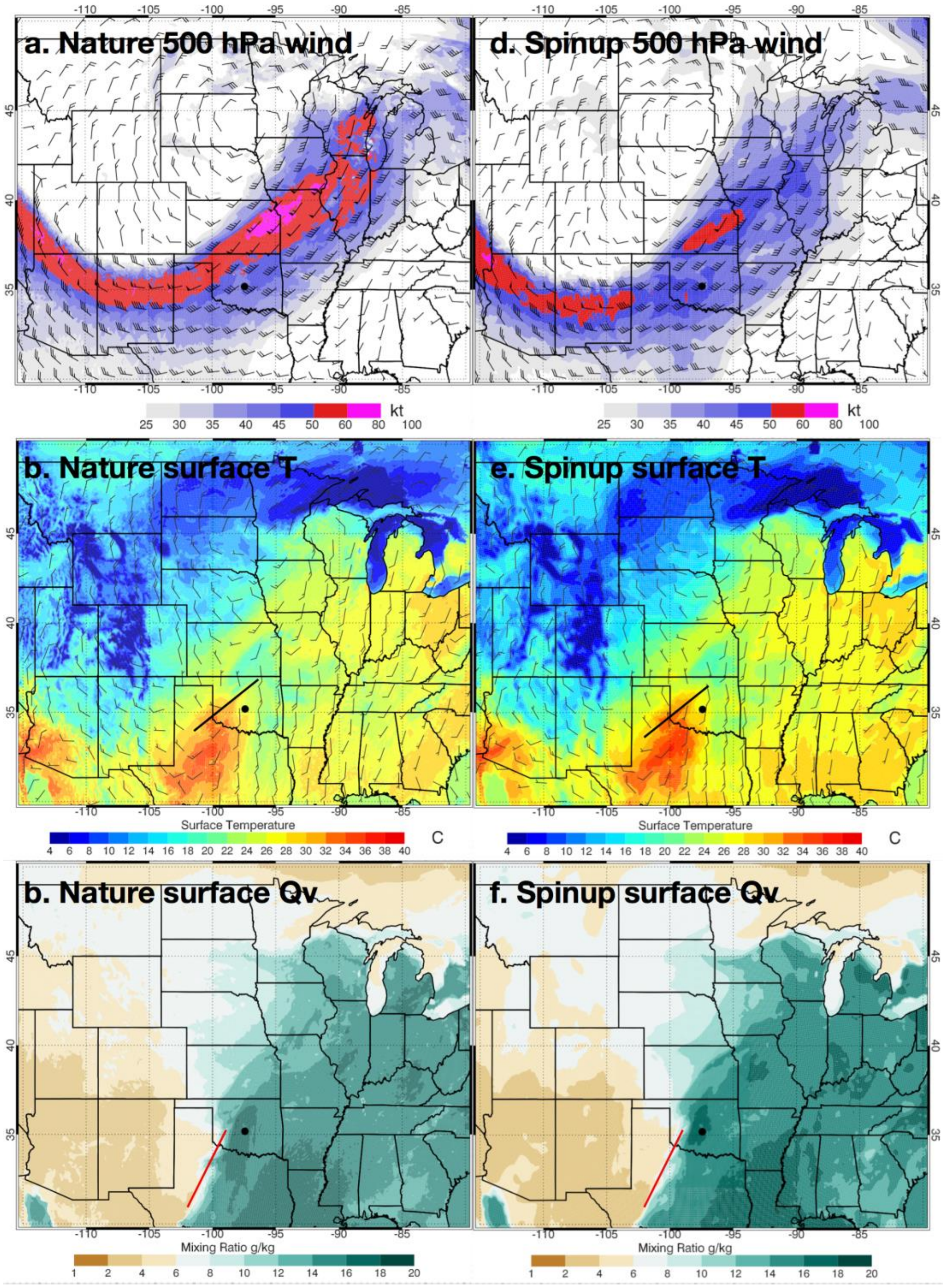

Figure 4. (a) Wind speed (knots) and direction at 500 hPa, (b) surface (2 m) temperature and 10 m winds, and (c) surface (2 m) water vapor mixing ratio for the nature run at 1800 UTC 20 May. Panels d, e, and f are identical, but for the spin-up ensemble mean analysis. The black dot indicates the location of Norman, OK (OUN) and the black and red lines indicate the approximate locations of the front and dryline respectively.

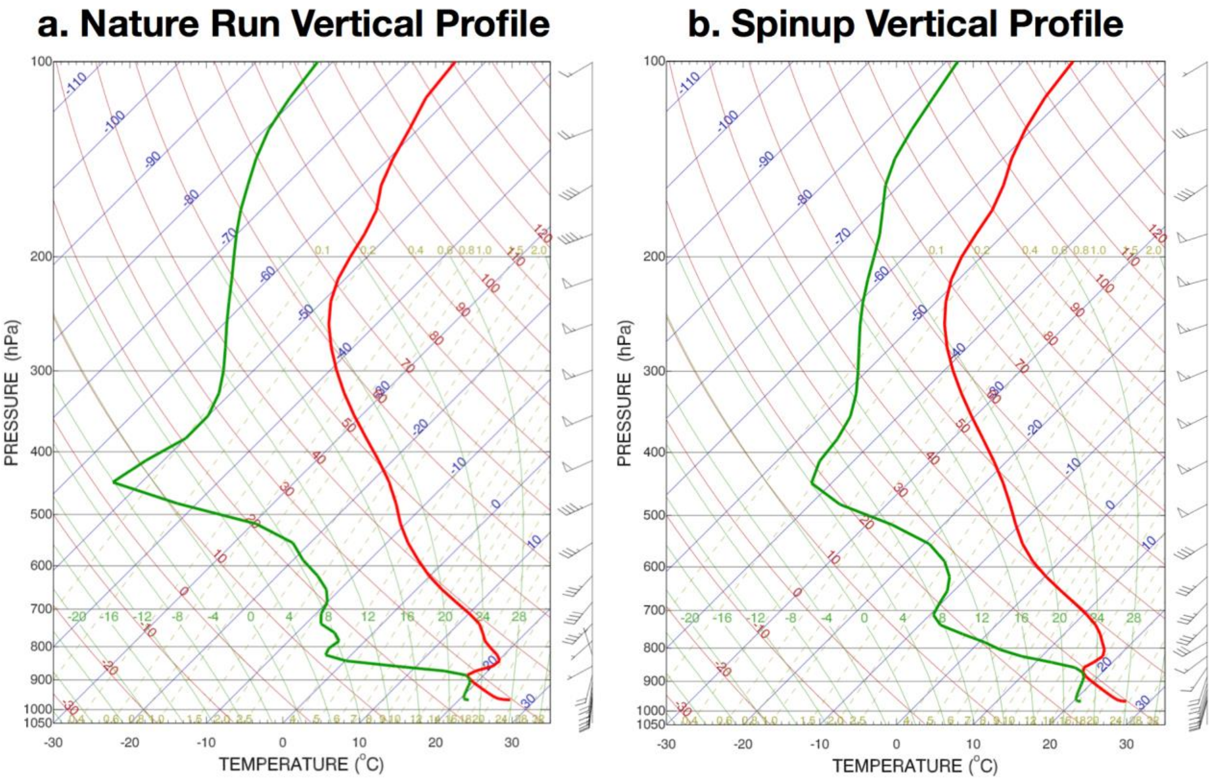

Figure 5. Temperature, dewpoint, and wind speed and direction profiles from (a) the Nature run and (b) the spin-up analysis located at Norman, OK (OUN) at 1800 UTC 20 May.

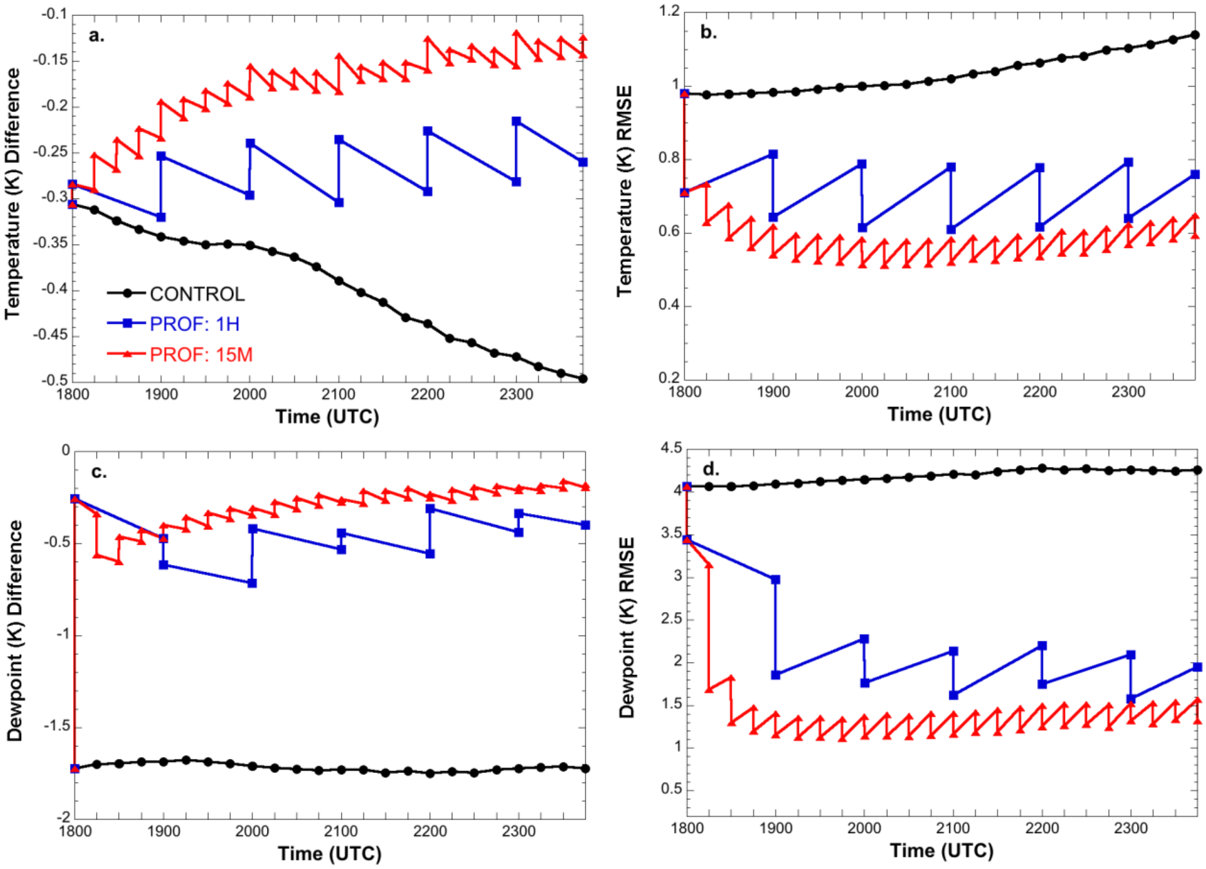

Figure 6. Mean (left panels) and RMSE (right panels) innovations (observations minus background) and residuals (observation minus analysis) for (top) temperature and (bottom) dewpoint temperature for CNTL, PROF1H, and PROF15M experiments for each assimilation cycle between 1800 UTC 20 May and 0000 UTC 21 May.

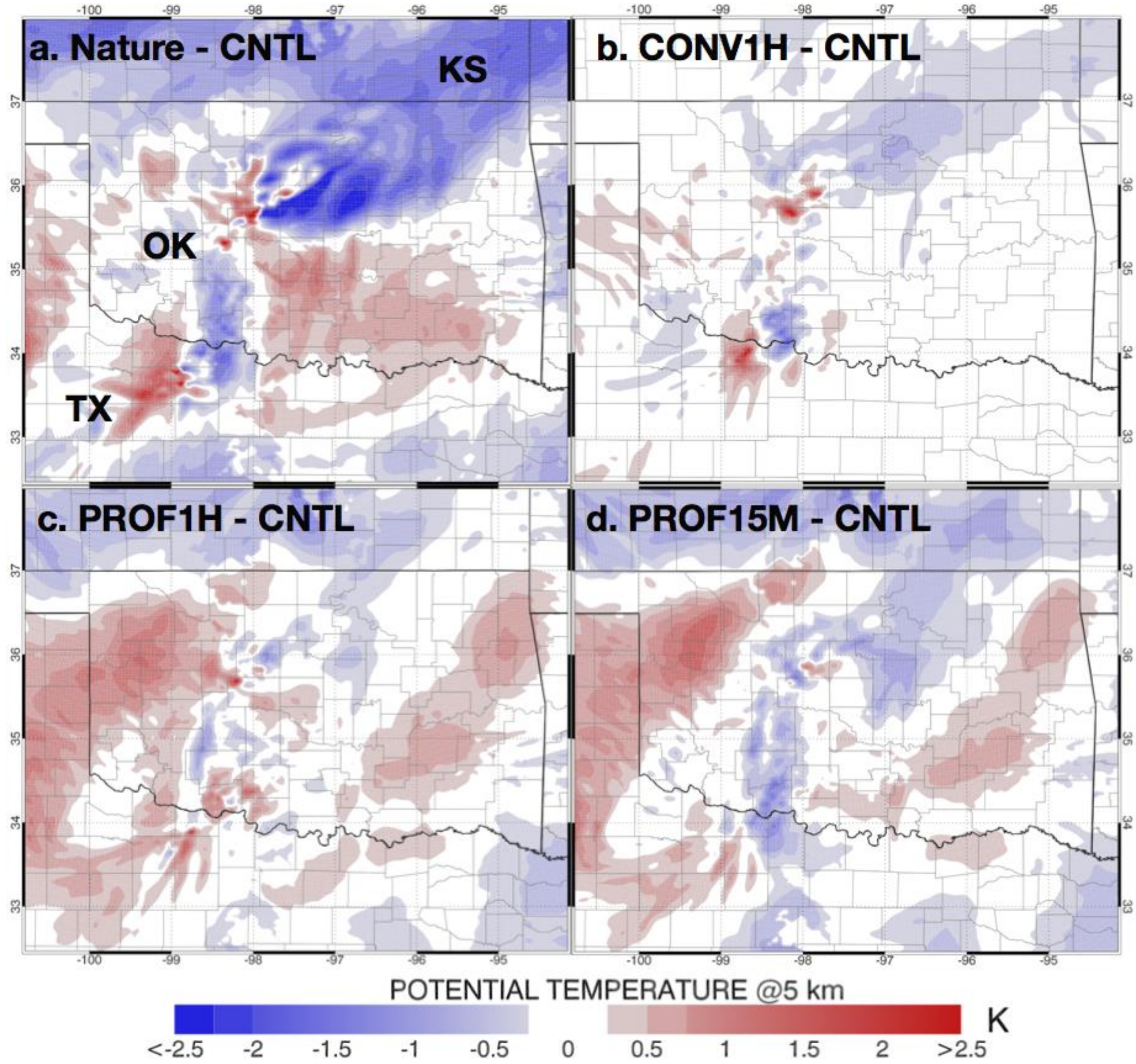

Figure 7. Potential temperature differences at 5 km and 2000 UTC 20 May with respect to the CNTL analysis for (a) the nature run (Nature), and for the (b) CONV1H, (c), PROF1H, and (d) PROF15M ensemble mean analyses.

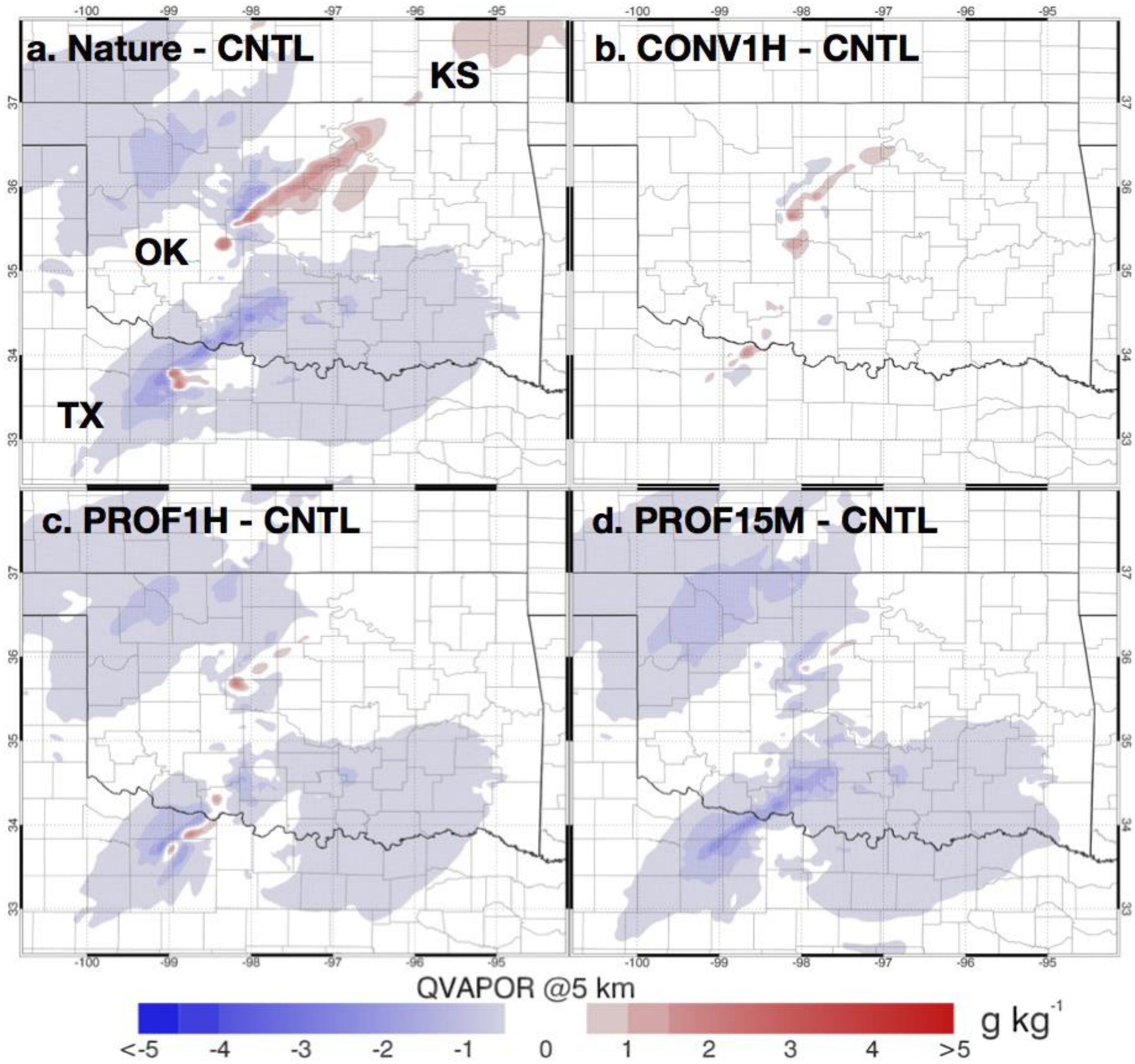

Figure 8. Water vapor mixing ratio difference at 5 and 2000 UTC 20 May with respect to the CNTL analysis for (a) the nature run (Nature), and for the (b) CONV1H, (c), PROF1H, and (d) PROF15M ensemble mean analyses.

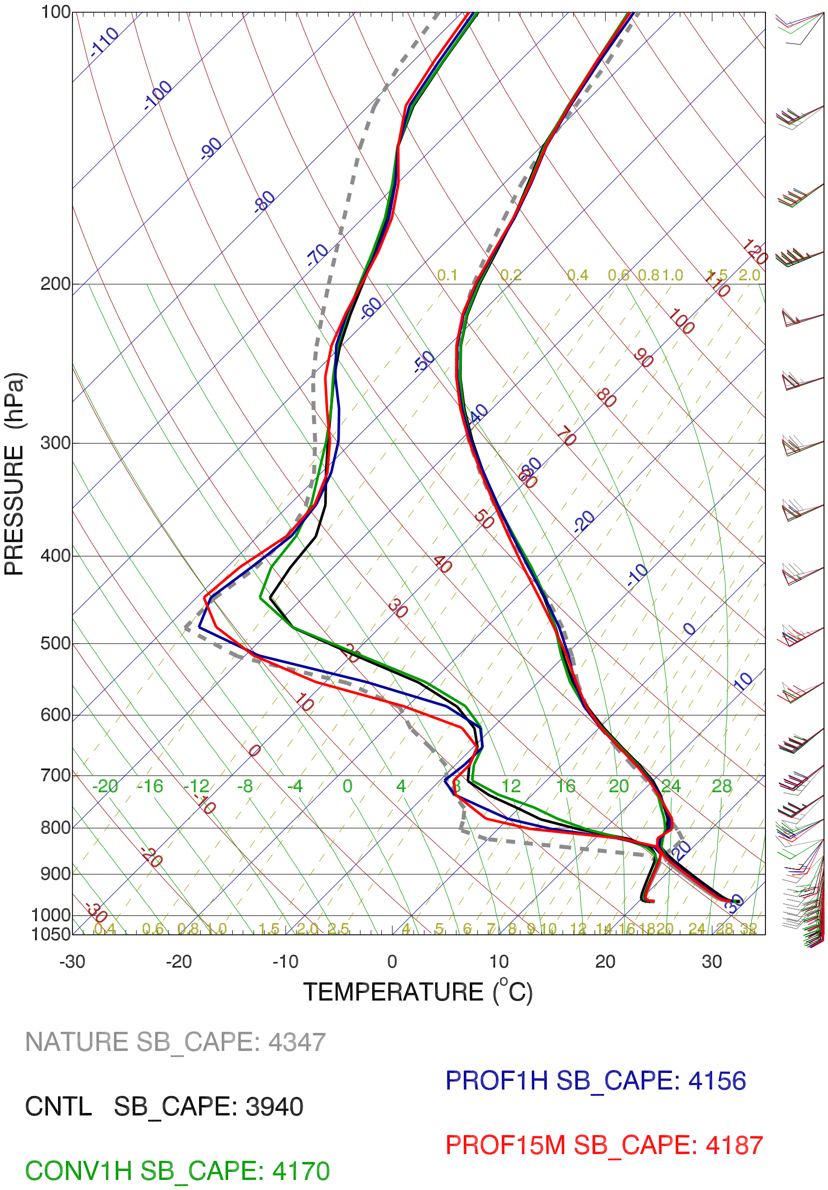

Figure 9. Vertical profile of temperature, dewpoint, and wind speed (kt) for each ensemble mean analysis and for the nature run at 2000 UTC at Norman OK (OUN).

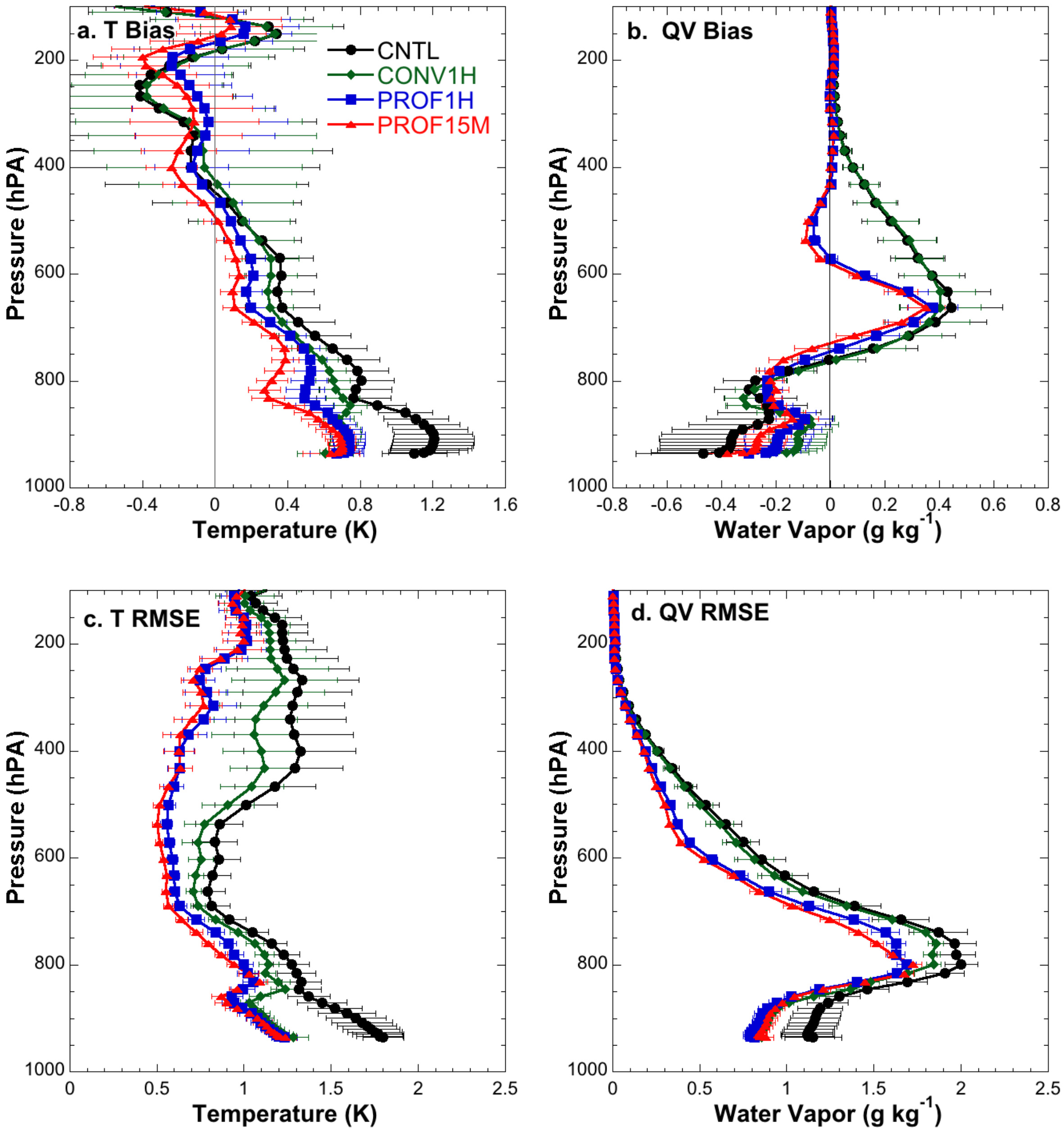

Figure 10. Vertical profiles of temperature and water vapor mixing ratio mean errors (top) and RMSE (bottom) for the 4 km nest for the 2000 UTC analysis. The mean and RMSE are calculated at each level for each ensemble member. Then the ensemble mean and standard deviations of these statistics are plotted as lines and error bars, respectively.

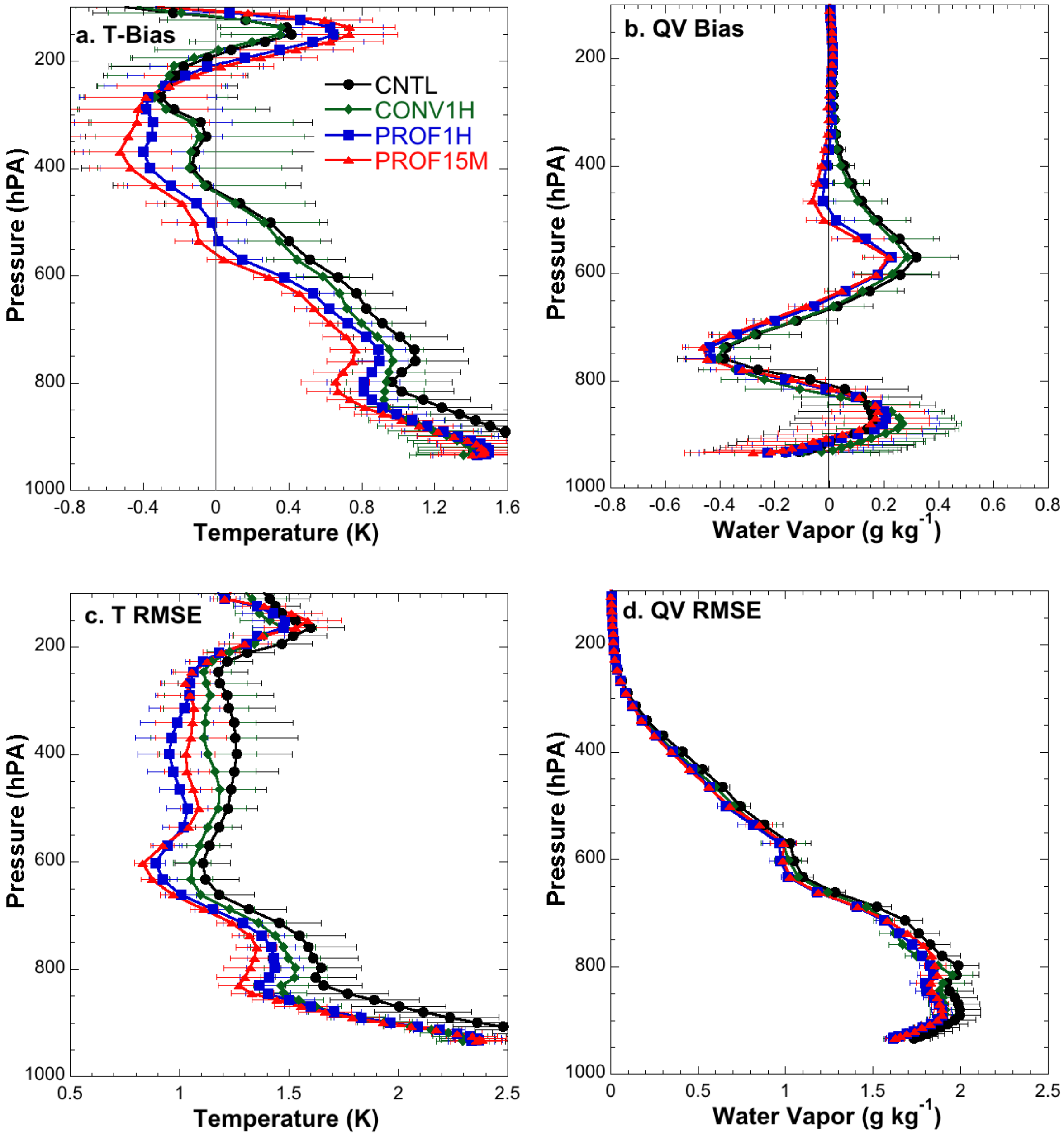

Figure 11. Same as Figure 10, but for a 4 hour forecast valid at 0000 UTC 21 May.

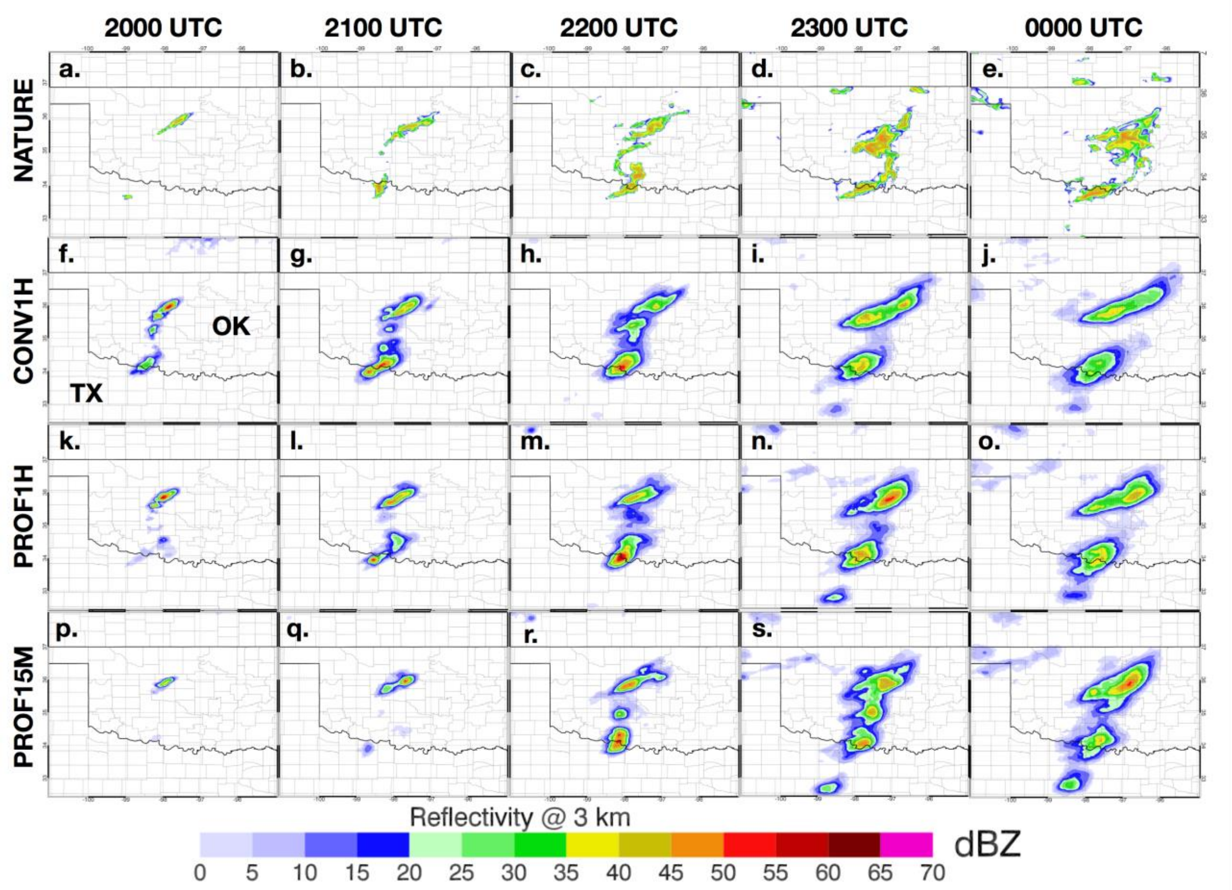

Figure 12. Simulated radar reflectivity at 3 km AGL from the nature run at 2000 (a), 2100 (b), 2200 (c, 2300 (d), and 0000 UTC (e) 20 May. Ensemble mean radar reflectivity at 3 km AGL for the 2000 UTC analysis and following forecasts at 2100, 2200, 2300, and 0000 UTC for CONV1H, PROF1H, and PROF15 experiments (f-t).

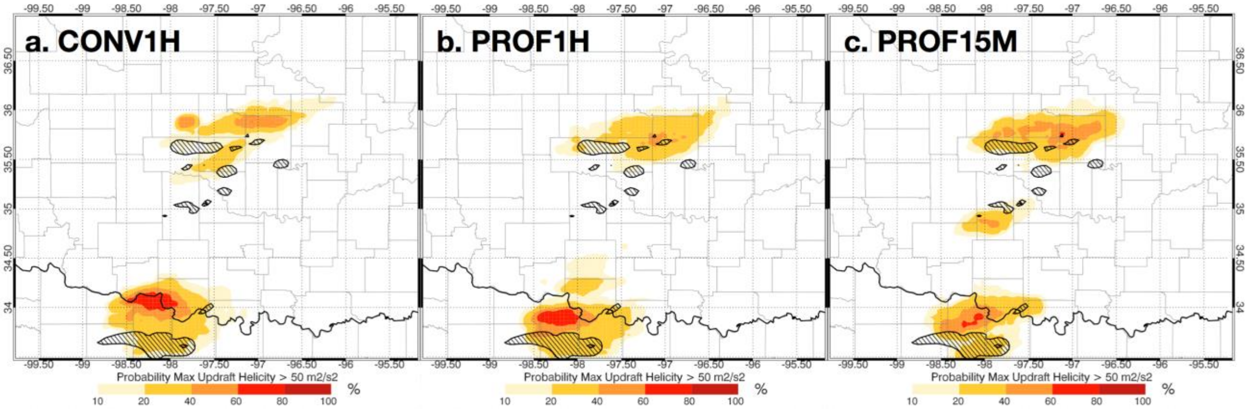

Figure 13. Ensemble estimated probability of 2-5 km updraft helicity integrated over a 4 hour forecast initiated at 2000 UTC 20 May greater than 50 m^2 s^{-2} for (a) CONV1H, (b) PROF1H, and (c) PROF15 experiments. In each panel the hatched areas indicate location of nature run helicity greater than 50 m^2 s^{-2} over the same time period.

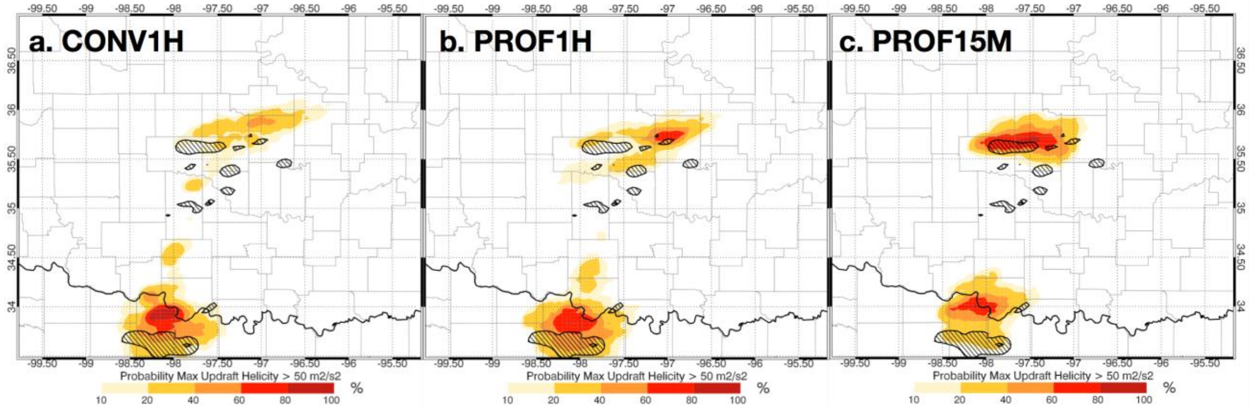

Figure 14. Same as Figure 14, but a for 3 hour forecasts initiated at 2100 UTC.

Tables

Sensor	**Observation Type**	**Error**
METAR	Temperature	1.75 K
METAR	Dewpoint	Lin and Hubbard (2004) model
METAR	U, V wind components	1.75 ms^{-1}
METAR	Altimeter	1.0 hPa
Radisonde	Temperature	0.8 – 1.5 K
Radisonde	Dewpoint	Lin and Hubbard (2004) model
Radisonde	U, V wind components	1.4 – 3.0 ms^{-1}
Radisonde	Altimeter	1.0 hPa
ACARS	Temperature	1.0 – 1.7 K
ACARS	U, V wind components	2.5 ms^{-1}

Table 1. Conventional observation types and errors used during this experiment.

		Parameterizations		
Member	**Cumulus**	**PBL**	**Radiation**	
			SW	LW
1	Kain-Fritsch	YSU	Dudhia	RRTM
2		YSU	RRTMG	RRTMG
3		MYJ	Dudhia	RRTM
4		MYJ	RRTMG	RRTMG
5		MYNN	Dudhia	RRTM
6		MYNN	RRTMG	RRTMG
7	Grell	YSU	Dudhia	RRTM
8		YSU	RRTMG	RRTMG
9		MYJ	Dudhia	RRTM
10		MYJ	RRTMG	RRTMG
11		MYNN	Dudhia	RRTM
12		MYNN	RRTMG	RRTMG
13	Tiedtke	YSU	Dudhia	RRTM
14		YSU	RRTMG	RRTMG
15		MYJ	Dudhia	RRTM
16		MYJ	RRTMG	RRTMG
17		MYNN	Dudhia	RRTM
18		MYNN	RRTMG	RRTMG

Table 2. “Multi-physics” options applied to the ensemble members to initialize ensemble members 1-18. This set of physics options also is applied to the same GEFS ensemble members, in reverse order, to initialize ensemble members 19-36 of the NEWS-e. All ensemble members use Thompson cloud microphysics and the Noah land surface model (Wheatley et al. 2015).

Assimilating synthetic hyperspectral sounder temperature and humidity retrievals to improve severe weather forecasts

Highlights:

1. Assimilates synthetic thermodynamic retrievals from hyperspectral instrument
2. Uses thermodynamic retrievals to sample the near storm environment
3. Improved model environment allows for improved short term forecasts of convection